Deep Learning Improves Global Satellite Observations of Ocean Eddy Dynamics

Scott A. Martin[1,*], Georgy E. Manucharyan[1], and Patrice Klein[2,3]

[1]School of Oceanography, University of Washington, Seattle, WA, 98195, USA
[2]Jet Propulsion Laboratory, California Institute of Technology, Pasadena, CA, 91125, USA
[3]Laboratoire de Météorologie Dynamique, École Normale Supérieure, Paris, 75230, France
[*]Corresponding author email: smart1n@uw.edu

Abstract

Ocean eddies help shape marine ecosystems, large-scale ocean circulation, and global climate through their non-linear interactions. Observing eddies poses a major challenge due to their chaotic evolution across a wide range of spatio-temporal scales. Satellite-derived estimates of surface ocean currents significantly distort and smooth eddies and, consequently, strongly underestimate the strength of non-linear eddy interactions. Here, we use deep learning to develop a new global estimate of surface currents from satellite observations, capturing ocean eddies with accuracy and resolution that surpasses state-of-the-art reconstructions. We achieved this by synthesising satellite observations of sea surface height with sea surface temperature across the Global Ocean using a single neural network that generalises across regions with diverse eddy dynamics. Our new reconstructions reveal dramatic changes in the inferred eddy dynamics in many regions, highlighting the existence of strongly seasonal non-linear eddy interactions. These eddy interactions transfer large amounts of kinetic energy from small to large scales, emphasising the prominent role of small-scale eddies in setting the seasonal cycle of kinetic energy in the ocean. Our study demonstrates that deep learning can dramatically improve our observations of ocean eddy dynamics from space, providing a new paradigm for satellite oceanography.

Mesoscale ocean eddies (vortices 50-300 km across) are a crucial component of the global ocean circulation and climate system due to their important role in the transport of heat and other tracers [1, 2, 3]. Strongly varying geographically and seasonally, mesoscale eddies are the dominant reservoir of kinetic energy (KE) in the Global Ocean [4]. The sources and sinks of mesoscale eddy KE are poorly constrained, especially the contribution from the transfer of KE between scales due to non-linear eddy interactions, a process known as the KE cascade [5, 6]. There is growing evidence that non-linear eddy interactions are strongly seasonal, leading to an upscale KE cascade (KE transfer from small to large scales) that is intensified in winter and spring [7, 8, 9, 10, 11, 12, 13, 14, 15, 16, 17]. The source of this seasonality has been hypothesised to be the injection of KE at submesoscales (O(1-10 km)) in the winter [18, 19, 20] followed by an upscale KE cascade [7, 8]. In turn, frontogenesis associated with the stirring of sea surface temperature (SST) by mesoscale eddies energises submesoscale currents with strong vertical velocities and associated heat and nutrient fluxes [21, 22, 23]. Quantifying these complex mesoscale-submesoscale interactions is crucial for the development of global climate models that do not resolve these processes [24, 25]. Non-linear eddy interactions and associated KE cascade are set by the relative vorticity and strain rate [5, 6], which are both difficult to constrain from observations since they are sensitive to the precise geometry and configuration of eddies. Since mesoscale eddies typically have strong surface expressions, global satellite observations are widely used to characterise eddy interactions [6].

Satellite altimetry observations allow the global estimation of eddies by mapping their expression in the sea surface height (SSH) field, which is used to estimate surface geostrophic currents [26]. Satellite altimeters measure SSH and resolve mesoscale eddies along each satellite's track [27] but leave large gaps between tracks that must be interpolated to diagnose the eddy field. Linear interpolation algorithms used to-date [28] poorly capture the chaotic evolution of ocean eddies between observations, causing smoothing and distortion of eddies [29]. This biases the diagnosed surface geostrophic currents, relative vorticity, and strain rate, potentially underestimating the strength of non-linear eddy interactions. There has thus been growing interest in developing improved mapping algorithms to create higher-resolution SSH maps [30, 31, 32, 33, 34, 35, 36, 37, 38, 39, 40].

Deep learning [41] is spurring rapid progress in climate modelling [42], numerical weather prediction [43, 44, 45], and increasingly in satellite oceanography [46, 34, 35, 36, 37, 38, 39, 40, 47, 48]. Recent studies show deep neural networks can be trained to estimate the SSH field from along-track observations using supervised learning on either synthetic data from numerical simulations [34, 35, 36, 37, 40] or real-world satellite observations [38, 39]. The advantage of this data-driven approach is that it allows the optimal mapping to emerge objectively from the data itself, unlike traditional linear methods [28, 29]. Deep learning also allows the use of observations of other surface ocean tracers to improve the SSH mapping between

altimeter observations. For example, SST can be a powerful predictor of SSH [37, 38, 39], highlighted by the close relationship between SSH and SST in idealised ocean turbulence theories [49]. Regional proof-of-concept studies showed deep learning yields state-of-the-art SSH maps, especially when SST is used [35, 36, 37, 38, 39, 40]. However, SSH mapping over the whole globe poses a significant challenge for deep learning algorithms as they need to generalise over a wide range of dynamical regimes, including strongly localised boundary currents, chaotic eddy fields, and fast-propagating large-scale waves.

In this study, we successfully reconstruct high-resolution global maps of SSH from satellite observations using deep learning. We trained a neural network exclusively on real-world satellite observations of along-track SSH and SST taken from small subdomains across the Global Ocean (Methods). We then merged subdomain SSH reconstructions to create global SSH maps that resolve ocean eddies with unprecedented accuracy and resolution (Methods). Our key technical contributions are two-fold. First, we demonstrated that a single neural network can generalise across different dynamical regimes to produce state-of-the-art global SSH maps. Second, we demonstrated that synthesising SSH and SST observations together significantly improves the mapping of SSH in almost all regions. These new high-resolution SSH maps dramatically improve our observations of eddy dynamics, providing new insight into the energy transfers between eddies of different scales.

State-of-the-art global SSH maps using deep learning

Our new global SSH maps show rich dynamical structures associated with western boundary currents, abundant mesoscale eddies in the extratropics, and large-scale equatorial waves in the tropics (Figure 1). Our mapping method ('SimVP SSH-SST') uses SST observations as an additional predictor to constrain the eddy field between altimeter observations and we compare it to the existing community-standard gridded SSH product ('DUACS') [28] (Methods).

The effective resolution (Methods) of our SSH maps is improved compared to DUACS throughout the Global Ocean, with a pronounced improvement in western boundary currents and the subtropics where we resolve wavelengths 30% smaller (Figure 2b,d and Extended Data Table 1). To evaluate the accuracy and resolution of SSH maps, we withheld observations taken by one altimeter from the input to the mapping and compared the mapped SSH to these withheld observations (Methods). The global root-mean-square error (RMSE) of the mapped SSH is 6% lower than DUACS, while reductions in the RMSE of small mesoscale signals (70-250km wavelengths) reach 20% in regions of intense eddy activity (Figure 2a,c,e and Extended Data Table 1). Our method also outperforms the recently-proposed 'MIOST' mapping method [31, 50, 51] (Methods) in almost all regions, especially for small mesoscale signals, making our method state-of-the-art in global SSH mapping (Extended Data Figure 1 and Extended Data Table 1).

SST observations improve the mapping of SSH throughout the Global Ocean (Figure 2f and Extended Data Table 1). To assess the utility of SST, we also trained a network that only used SSH observations and compared its performance to the one that additionally used SST. The mapping of small mesoscale signals is improved using SST, especially in the extratropics where mesoscale SSH and SST are correlated [52] (Figure 2f and Extended Data Table 1). The use of SST is critical when few altimeters are available (Extended Data Table 2). While observations from 6 satellite altimeters were used to create the maps compared above, for much of the altimetry era there were only 2 altimeters operational. This sparsity of observations causes eddies in DUACS, which does not utilise SST, to be severely smoothed. We evaluated our network using only 2 altimeters as input and found that in most regions SimVP SSH-SST with just 2 altimeters yields higher-resolution SSH than DUACS achieves with 6 (Extended Data Table 2). This highlights the power of using deep learning and SST to extract maximum value from the 30-year altimetry record.

Our neural network maps SSH across all regions despite their distinct regional dynamics, unlike prior studies which trained bespoke region-specific networks [35, 36, 37, 38, 39, 40]. Seeing a wide range of dynamical regimes during training forces the network to generalise, which should make it robust against local regime changes induced by the inter-annual variability of large-scale currents. While bespoke regional networks [38, 40] in the Gulf Stream offer marginally improved SSH mapping compared to our global network [53] (Extended Data Table 3), fine-tuning on a smaller set of observations from the Gulf Stream Extension (Methods) brings our network's performance close to state-of-the-art regional networks (Extended Data Table 3).

Improved physical realism of mesoscale eddies

Surface geostrophic currents (Methods) from our maps are more accurate when evaluated with in-situ observations. We compared geostrophic currents from the SSH maps to surface drifter observations (Methods) and found our maps reduce the RMSE significantly across the Global Ocean, especially in the subtropics where the RMSE is reduced by 20% compared to DUACS (Extended Data Figure 2). Discrepancies between the mapped currents and drifter observations are due to both the accuracy of the mapped geostrophic current and the degree to which real-world currents are in geostrophic balance, since drifters also sample Ekman and other ageostrophic currents. Nonetheless, the large reduction in RMSE demonstrates the significant improvement in the mapped currents.

To demonstrate the radically improved physical realism of reconstructed mesoscale eddies, we calculated relative vorticity and strain rate from the mapped surface currents, which characterise the rotation and deformation of submesoscale currents by mesoscale eddies (Methods). These key diagnostics of eddy dynamics are strongly sensitive to the sharpness of the velocity gradients around eddies which are better represented in our higher-resolution maps. Comparing the relative vorticity and strain rate with those from the lower-resolution DUACS product, we found dramatic qualitative differences (Figure 3b,c,d and Supplementary Movie). Our relative vorticity fields show an abundance of small mesoscale eddies with clearly-defined boundaries between eddies and movies of relative vorticity show eddy evolution more reminiscent of numerical simulations of ocean turbulence (Figure 3b,c and Supplementary Movie). Our maps also better capture the fast evolution of western boundary currents which are well-observed with SST due to their large across-current temperature gradients. Zooming in on small clusters of eddies reveals that the strain rate between eddies is increased in our maps relative to DUACS, highlighted by regions where the Okubo-Weiss quantity (Methods) is positive (Figure 3d). Increased strain rate has important implications for eddy dynamics since it is associated with enhanced formation of submesoscale fronts [21, 22] and a stronger cascade of energy between scales [5].

In many regions, our improved maps reveal fundamentally different eddy dynamics. For example, in the Subtropical North Pacific (defined in Extended Data Table 1), eddies in DUACS exhibit a uniform westward drift (Supplementary Movie), which was previously attributed to the beta drift phenomenon [26]. However, this uniform drift is absent in our maps, and a strongly interacting eddy field emerges. The uniform drift is likely an artefact of *a priori* assumptions in the DUACS interpolation method, namely the prescription of mean eddy propagation velocities (see Eq. 6 in Methods). This highlights the drawbacks of using human-designed covariance models in linear interpolation methods [54, 28] compared to a fully data-driven deep learning approach.

Seasonality of mesoscale eddy dynamics

A distinct seasonality in eddy dynamics emerges in our maps that was largely absent in DUACS. The mean eddy kinetic energy (EKE) at small mesoscales (wavelengths below 250km) peaks in winter and spring when it is 50-100% higher than in DUACS throughout the subtropics and western boundary currents (Figure 4a,b, Extended Data Figure 3a,b, and Extended Data Figure 4). The eddy strain rate is also enhanced throughout the subtropics by 50-100% in winter and spring but matches DUACS more closely in summer and autumn (Figure 4c,d and Extended Data Figure 3c,d). Importantly, the enhanced EKE and strain rate conspire to nearly triple the strength of non-linear eddy interactions compared to DUACS (Methods) in winter and spring in the subtropics (Figure 4e,f, Extended Data Figure 3e,f and Extended Data Figure 5). This seasonality was previously obscured since small mesoscale eddies that proliferate in winter and spring are below DUACS's resolution limit (Extended Data Table 1).

We highlight this newly-resolved seasonality by focusing again on the Subtropical North Pacific which was the subject of prior studies [8]. The kinetic energy (KE) wavenumber spectrum has a shallower slope ($\approx k^{-2}$) in winter and spring than in summer and autumn ($\approx k^{-3}$) (Figure 5a), meaning energy is concentrated at small scales in winter and spring with an associated springtime increase in the strength of relative vorticity and strain rate (Extended Data Figure 6). The large-scale KE (scales $>$125 km) peaks in May-July, whereas small-scale KE ($<$125km) peaks earlier in March-April, leading the large-scale peak by 2 months (Figure 5b). The summertime large-scale KE peak could ultimately be driven by KE generated at submesoscales during winter that undergoes an upscale KE cascade to mesoscales during spring [7, 8]. However, diagnosing the KE cascade through global observations presents a major challenge as it requires accurately resolving eddies across a wide range of scales. Using low-resolution gridded products like DUACS to diagnose the KE cascade [55] can lead to substantial biases and artefacts [5]. Below, we reassess the seasonal upscale cascade hypothesis [7, 8] using our higher-resolution surface geostrophic currents.

Seasonal transfer of kinetic energy from small to large scales

The diagnosed KE cascade from our maps (Methods) is upscale in a range of regions and is strongly seasonal (Figure 5 and Extended Data Figure 7). Focusing again on the Subtropical North Pacific, the KE cascade there is upscale (negative) at all scales and is strongest in the spring (Figure 5c). Even though some KE sources and sinks cannot be derived from surface geostrophic currents (Methods), the magnitude of the diagnosed upscale cascade is more than sufficient to drive the seasonal increase in large-scale KE over winter and spring (Figure 5d). In sharp contrast, the cascade in the DUACS maps does not sufficiently strengthen in winter/spring to explain the observed peak in large-scale KE (Figure 5d and Extended Data Figure 7). The dramatic underestimation of the KE cascade in DUACS is an artefact of the smoothing of small-scale eddies, which obscured the existence of a strong seasonal upscale cascade. The same analysis in the Subtropical South Pacific (Extended Data Figure 7) reveals a similar picture, suggesting that this seasonal upscale cascade is widespread throughout the subtropics. Near western boundary currents, like in the Kuroshio and Gulf Stream Extensions, there is also a large difference in the cascade between the maps, but the role of the cascade in driving seasonality at larger scales is less clear. This may in part be due to strong variability associated with the unstable western boundary currents (Extended Data Figure 7).

While our maps resolve smaller eddies, they still smooth scales below O(100km) (Extended Data Table 4), so the strength of the upscale cascade at smaller scales is likely underestimated. In addition, unbalanced motions at smaller scales, which cannot be diagnosed using geostrophy, could also impact the cascade [56, 10, 11]. Hence, direct confirmation of the hypothesis that KE generation at submesoscales plays a significant role in the seasonality of mesoscale eddies [7, 8] requires global submesoscale-resolving observations [6, 57], nonetheless, our results are broadly consistent with this picture in the subtropics.

Deep learning as a new paradigm for satellite oceanography

Our high-resolution SSH maps generated using deep learning represent a large stride forward for the global observation of ocean eddies. This a valuable dataset for future studies of eddy dynamics, including scale interactions [6], explorations of eddy parameterisations [58], inference of vertical velocities and subsurface currents [59, 46], and the cumulative impacts of mesoscale eddies on climate and marine ecosystems. Deep learning methods for satellite oceanography are still in their infancy. Nonetheless, this study demonstrates that deep learning can be used to create state-of-the-art global datasets and provides a road-map for the development and operationalisation of data-driven maps of other essential climate variables [47, 48].

We anticipate that further improvements of ocean eddy observations can be achieved by incorporating increasingly high-resolution training data from either numerical simulations or next-generation satellite altimeters. Using synthetic observations from numerical simulations during training has been shown to improve SSH mapping in regional studies [40]. However, this approach requires caution as this blurs the boundary between the potentially biased numerical models and observations. In parallel, continued development of observation-only learning [38, 39] is needed to provide independent observation-only datasets to evaluate numerical models. We anticipate such efforts will benefit from using submesoscale-resolving two-dimensional snapshots of SSH taken by SWOT, the first wide-swath altimeter [57]. SWOT observations could help better characterise the KE cascade in the currently unresolved submesoscale range [6]. However, using this data will present new challenges due to a mismatch between the fast-evolving submesoscale dynamics and SWOT's long orbital return times [60, 61].

This study provides strong motivation for the future development of neural networks with more expressive architectures that can synthesise multi-modal satellite observations to push towards global submesoscale-resolving surface ocean state estimates. This will require a significant increase in the scale of neural network architectures and training datasets due to the required order of magnitude increase in spatial resolution. The neural network used in this study is dwarfed in scale and expressivity by cutting edge architectures used in computer vision [62] and increasingly in weather and climate [44, 63]. A coordinated effort is needed to develop 'foundation models' to address the grand challenges of the upcoming era of submesoscale-resolving satellite oceanography.

Methods

Sea surface height and surface geostrophic currents

At large temporal and spatial scales, ocean currents are approximately in geostrophic balance [64], meaning that currents arrange themselves such that the horizontal pressure gradient force is balanced by the Coriolis force. Surface pressure in the ocean can be directly related to sea surface height anomaly (SSH), allowing surface current velocity to be estimated from satellite altimeter observations of SSH. The surface currents are proportional to the spatial gradients of the SSH field

$$(u_g, v_g) = \frac{g}{f}\left(-\frac{\partial \eta}{\partial y}, \frac{\partial \eta}{\partial x}\right), \tag{1}$$

where u_g and v_g are the Eastward and Northward geostrophic surface currents respectively, g is the acceleration due to gravity, η is the SSH, f is the local Coriolis frequency, and x and y are zonal and meridional coordinates respectively. This relation breaks down near the Equator where f approaches zero, so we do not calculate surface geostrophic currents within the equatorial band (5°S to 5°N).

Satellite datasets

The along-track SSH observations used in this study are those processed by the Data Unification and Altimeter Combination System (DUACS) and distributed by the Copernicus Marine Environmental Service (CMEMS) [65, 66]. Specifically, we use the unfiltered, Level 3 sea level anomaly observations. At Level 3, the observations have been corrected for atmospheric effects, the barotropic tide has been removed, and the data has been adjusted to ensure consistency between the different altimeter missions.

We use the Multi-scale Ultra-high Resolution (MUR) SST analysis product to provide a gridded estimate of SST as an additional predictor variable in the mapping of SSH that combines observations from a wide range of satellite infrared and microwave radiometer observations [67, 68]. While this product is distributed on a 1/100th degree grid, the spatial scales resolved vary in space and time due to satellite sampling and cloud cover.

Formulating SSH interpolation as a supervised deep learning problem

After appropriate data pre-processing, SSH interpolation can be viewed as a video in-painting problem with an extremely high missing pixel rate ($\sim 90\%$) [34, 38, 35]. We first extract satellite altimeter SSH observations in some restricted spatiotemporal subdomain within which we seek to estimate the full SSH field. This subdomain is discretised into a regular grid in space and time onto which the observations are bin-averaged; empty voxels are padded with zeroes. This data can now be considered as a heavily-masked video, and our objective is to predict the corresponding full, unmasked video using a deep learning neural network. The objective minimised during training is the mean squared error (MSE) between the prediction and the ground-truth. When training on real-world altimetry observations, there is no full unmasked ground-truth dataset to use during training. We overcome this by randomly withholding some of the altimetry observations from the input and calculating the MSE only at the locations of these withheld observations [38]. Co-located estimates of gridded SST are used as an extra predictor variable by averaging them onto the same local grid and presenting this (unmasked) video as an additional input to the neural network. The dimensions of the local grid on which we map SSH were chosen to be 128x128 in the spatial domain with 7.5km grid resolution (latitude, longitude coordinates are first projected onto a local orthonormal grid to avoid distortion), and 30 frames in the temporal domain with 1 day grid resolution. Rationalisation and validation of these choices is given in our previous study [38]. To train our network, we generated a training dataset of 1 million local subdomains centred on random points in space and time throughout the Global Ocean. The data are split in the temporal domain to ensure well-separated training, validation, and testing datasets, with 2019 being withheld for testing, and the remaining years from 2010-2022 split into non-overlapping training and validation periods (Extended Data Figure 8).

The mapping errors grow away from the centre of the local spatiotemporal grid due the omission of observations outside the local subdomain, therefore to produce the optimal reconstruction we use only the middle day of the predicted time-series during inference and points close to the edge of the subdomain are given low weight in our algorithm for merging subdomain reconstructions to produce a global SSH estimate .

Deep learning neural network architecture

After formulating SSH interpolation as discussed above, we are to free to use any sequence-to-sequence video prediction model from the extensive computer vision literature. To ensure we employed a state-of-the-art architecture, we chose the top-performing architecture on the Moving MNIST video prediction benchmark [69] at the time of our study, SimVP [70, 71]. SimVP is built up of three modules: a spatial encoder that learns to encode each frame of the input independently in some lower-dimensional latent space, a temporal translator that learns both spatial and temporal dependencies from the latent space, and a spatial decoder that decodes the latent space into the predicted video frames. Unlike widely-used recurrent architectures, such as ConvLSTM [72], SimVP uses convolutional neural networks (CNNs) for all three modules. Our architecture is as described in Tan et al. [71], where the temporal translator module is a gated spatio-temporal attention translator, which uses large convolutional kernels to imitate the attention mechanism allowing the translator to adaptively select informative features from the latent space. Compared with Tan et al., we removed the skip connection from the first layer of the spatial encoder to the final layer of the spatial decoder since the extreme sparsity of the input SSH frames led to the appearance of artifacts in the output coinciding with the input altimeter tracks. To synthesise SSH and SST, we use a separate spatial encoder for each variable before concatenating the encoded SSH and SST in the channel dimension and passing this to the temporal translator. Except for the temporal translator, the architecture used here is similar to the ConvLSTM-based architecture used in our earlier regional SSH mapping study [38]. During early testing we found SimVP to outperform ConvLSTM in global SSH reconstruction, which requires a more expressive architecture due to the diverse range of dynamical regimes, and its performance (when trained on global data) is comparable to our previously published values for ConvLSTM in the Gulf Stream despite the latter being trained exclusively on this region (Extended Data Table 3). Each network was trained for 50 epochs using the OneCycle learning rate scheduling policy, the Adam optimiser, and with drop-out and drop-path probabilities of 0.2 and 0.15 respectively which were selected after performing hyper-parameter optimisation on 10% of the training data. Each training on the global training dataset took 7 days on a single node with four Nvidia V100 GPUs.

Merging subdomain reconstructions to create global SSH product

Our neural network predicts gridded SSH on subdomains of size 960x960km. To produce a global gridded SSH estimate we use the trained network to predict SSH on 5615 subdomains with centres chosen to be approximately equally spaced by a distance of 250km throughout the Global Ocean. There is therefore substantial overlap between neighbouring subdomains. To merge the subdomain reconstructions into a single global SSH estimate we use the kernel-weighted averaging method described in Appendix A of Callaham et al. [73] and outlined below.

The global 2D SSH estimate, $\widehat{\mathbf{x}}$, defined on a regular 1/10th degree grid, is computed from the k subdomain estimates

through

$$\widehat{\mathbf{x}} = \sum_{i=1}^{k} \Phi_i \odot \widehat{\mathbf{x}}_i, \tag{2}$$

where Φ_i is a normalised weighting kernel for each subdomain, $\widehat{\mathbf{x}}_i$ are the subdomain SSH estimates, and $\odot$ denotes the Hadamard (i.e. element-wise) product between two matrices. Note that each $\widehat{\mathbf{x}}_i$ and Φ_i are filled with zeroes at all points covered by land or sea ice and at points lying outside the subdomain. All matrices were first regridded to the regular 1/10th degree grid from the original, irregular subdomain grid using bi-linear interpolation. Each weighting kernel is taken to be a Gaussian centred on the the corresponding subdomain

$$\Phi_i(\mathbf{r}) = \frac{1}{N(\mathbf{r})} \exp\left(-\frac{|\mathbf{r}-\mathbf{r}_i|^2}{L^2}\right), \tag{3}$$

where $\mathbf{r}$ is the position of the point being estimated, $\mathbf{r_i}$ is the position of the subdomain centre, L is the characteristic width of the Gaussian kernel, and $N(\mathbf{r})$ is a normalisation factor chosen such that

$$N(\mathbf{r}) = \sum_{i=1}^{k} \Phi_i(\mathbf{r}). \tag{4}$$

The mapping errors in the subdomain reconstructions are expected to increase away from the centre of the subdomain due to the omission of observations outside the subdomain in the mapping. Thus, for minimising the error of the global estimate maximising the number of subdomains is desirable. The choice to space the subdomains by 250km was made as the minimum spacing our computing resources would reasonably permit (merging the subdomain reconstructions for a single day takes ~ 3 minutes per CPU worker at this spacing). Given this subdomain spacing, the value of L was tuned so as to minimise the mapping error for the global estimate. We found the errors to be only weakly dependent on kernel width for widths within reasonable bounds, the results presented in the manuscript were obtained using $L = 250$km. All first- and second-order spatial derivatives of the SSH field were computed first on the orthonormal subdomain grid using smooth noise-robust differentiator kernels (discussed in Arbic et al. [74]) before being merged using the above algorithm to avoid the appearance of high-frequency numerical artefacts [38] (a similar result can be obtained by a simple low-pass filtering of the mapped SSH).

Regional fine-tuning experiment

In Extended Data Table 3 we show that SimVP SSH-SST trained on global observations can be fine-tuned for regional applications to bring its performance closer to that of state-of-the-art regional schemes [40, 38]. The global model was trained on 1 million training examples drawn randomly from the Global Ocean. During fine-tuning we started training from the converged global model using the Adam optimiser with a fixed learning rate parameter of 10^{-4} on a smaller training set of 100 thousand examples drawn randomly from the Gulf Stream (as in our previous study [38]) and continued training until the validation loss stopped improving. This fine-tuning took 12 hours on a single node with four Nvidia V100 GPUs. The results presented in the rest of the study use only the global trained model to limit the computational resources of the method, but in future an ensemble of bespoke regional models could be fine-tuned to further optimise the SSH mapping in each region if these maps were produced operationally by a data centre. Since previous studies used a different test year, 2017, in the Gulf Stream [53], we swapped 2017 and 2019 in our training-validation-testing split (Extended Data Figure 8) to ensure 2017 was withheld during training and cross-validation (both the global and regional training were done with this updated split).

SSH map evaluation and inter-comparison

To evaluate the accuracy and resolution of the SSH signals resolved by different mapping methods, we employ an 'observing system experiment' (OSE) in which each method is used to generate global gridded SSH estimates using all but one of the available satellite altimeters which is then used as an independent validation of the mapped signal. Since the existing operational SSH products are only distributed using all available altimeters, performing an OSE would typically involve re-implementation of all existing methods, which would be challenging in the case of SSH mapping since the covariance parameters used to create the community-standard DUACS product are not publicly-available. To address this, in recent years a series of 'Ocean Data Challenges' have been developed [33]. In each challenge a common mapping OSE problem is defined, developers of different methods implement their method and post their results, allowing a transparent performance benchmark.

To evaluate our global product, we use the recently-created global OSE challenge: '`2023a_SSH_mapping_OSE`' [75]. In this challenge, each method is used to create 1 year (2019) of global gridded SSH estimates using SSH observations from the satellites Jason 3, Sentinel 3A, Sentinel 3B, Haiyang-2A, Haiyang-2B, and Cryosat-2, while observations from the satellite

Saral/Altika are withheld for validation. While the validation observations only sample the maps along 1D tracks, aggregating over a full year allows robust, geographically-varying error statistics to be found.

We present three SSH error metrics using the withheld altimeter, each averaged over the full year and binned into 1° bins: the root-mean-square error (RMSE) between the mapped and observed signals, the RMSE after applying a 70-250km along-track band-pass spatial filter to both the observed and mapped signals along the satellite tracks to highlight the maps' ability to map small mesoscale eddies, and the effective spatial resolution of the mapped signal. The effective resolution is found by taking along-track segments of the withheld altimeter observations along with the mapped values at these locations and calculating the signal-to-noise ratio as a function of wavelength by dividing the power spectral density of the mapping errors by that of the observations. Concretely, the 'effective spatial resolution' is taken to be the wavelength at which the signal-to-noise ratio between the observed and mapped signals drops below 0.5 [29].

To evaluate the surface currents inferred from each SSH map, surface drifter observations from the CMEMS global in-situ water velocity product [76] are used. Surface drifter observations are not used in the generation of any of the surface current maps presented here, so they are an independent validation dataset. We present geographically averaged velocity RMSE values for each method.

At the time of writing, three other SSH mapping methods have been implemented world-wide and all are available in the data challenge for evaluation: DUACS [54, 28], MIOST (geostrophic) [31], and MIOST (geostrophic + equatorial waves) [51]. DUACS (Data Unification and Altimeter Combination Service) is the community-standard gridded SSH product that is distributed operationally by CMEMS. The DUACS system uses a linear optimal interpolation (OI) formulation [77], in which an *a priori* model is prescribed for how SSH covaries in space and in time, then the missing values are estimated using the best linear least-squares estimator. The assumed covariance, C, is

$$C(r,t) = \left(1 + ar + \frac{1}{6}(ar)^2 - \frac{1}{6}(ar)^3\right)\exp(-ar)\exp\left(\frac{-t^2}{T^2}\right), \tag{5}$$

where t is the temporal separation of the observation and mapped point under consideration, T is a prescribed de-correlation time-scale, $a = 3.337$, and

$$r = \sqrt{\left(\frac{dx - C_{px}t}{L_x}\right)^2 + \left(\frac{dy - C_{py}t}{L_y}\right)^2}, \tag{6}$$

where L_x and L_y are prescribed de-correlation length-scales in the zonal and meridional directions, dx and dy are respectively the zonal and meridional separation of the observation and mapped point under consideration, and C_{px} and C_{py} are prescribed propagation velocities. The de-correlation scales and propagation velocities are allowed to vary with geographical location and the values used are not publicly available but have been tuned over many years to best map mesoscale ocean features globally. The MIOST (Multiscale Interpolation Ocean Science Topography) mapping method extends the linear mapping framework, using a wavelet decomposition to allow the construction of multiple independent components of the assumed covariance model [50, 51]. MIOST (geostrophic) uses a single component in the covariance model intended to represent the geostrophically balanced component of SSH evolution, while MIOST (geostrophy + equatorial waves) adds an additional component to model the propagation of tropical instability waves and Poincare waves near the equator.

Season definitions

Wherever results are split by season in this study we define those seasons in the Northern (Southern) Hemisphere: winter is January-March (July-September), spring is April-June (October-December), summer is July-September (January-March), and autumn is October-December (April-June).

Eddy kinetic energy

The kinetic energy, KE, per unit volume of the surface currents is calculated from the surface geostrophic current maps

$$\mathrm{KE} = \frac{\rho_0}{2}\left(u_g^2 + v_g^2\right), \tag{7}$$

where ρ_0 is a reference density taken to be $1025 kgm^{-3}$. The eddy kinetic energy, EKE, is defined as the time-varying component of the KE

$$\mathrm{EKE} = \mathrm{KE} - \overline{\mathrm{KE}}, \tag{8}$$

where $\overline{\mathrm{KE}}$ is the time mean of the KE.

To highlight the difference in small-scale EKE between the maps we also calculate the EKE of the surface currents after the application of a 250km high-pass filter.

Relative vorticity, strain rate, and Okubo-Weiss quantity

While first order spatial derivatives of SSH give the velocity of the geostrophic currents, second order spatial derivatives quantify the deformation and rotation induced by the flow. The relative vorticity, ω, describes the local rotation of the fluid (that is, how a patch of tracers would tend to rotate if placed at a point within the flow)

$$\omega = \frac{\partial v_g}{\partial x} - \frac{\partial u_g}{\partial y} = \frac{g}{f}\nabla_h^2 \eta, \tag{9}$$

where ∇_h^2 is the horizontal Laplacian.

Meanwhile, the strain rate, s, defines the deformation of fluid elements by the flow (that is, how a patch of tracers would change shape due to the flow)

$$s = \sqrt{s_n^2 + s_s^2} \tag{10}$$

where s_n is the normal component of the strain

$$s_n = \frac{\partial u_g}{\partial x} - \frac{\partial v_g}{\partial y} = -2\frac{g}{f}\frac{\partial^2 \eta}{\partial x \partial y}, \tag{11}$$

and s_s is the shear component

$$s_s = \frac{\partial v_g}{\partial x} + \frac{\partial u_g}{\partial y} = \frac{g}{f}\left(\frac{\partial^2 \eta}{\partial x^2} - \frac{\partial^2 \eta}{\partial y^2}\right). \tag{12}$$

A high strain rate is associated with the stretching of patches of fluid, is common in the areas between eddies, and is associated with the generation of submesoscale filaments through frontogenesis [21] and strong transfer of kinetic energy between scales [5]. Whereas strong relative vorticity (either positive or negative) is associated with coherent, persistent eddies and is typical in the cores of eddies.

The relative importance of relative vorticity and strain rate at each point in the fluid can be described using the Okubo-Weiss quantity [78, 79],

$$W = s^2 - \omega^2, \tag{13}$$

which is positive when strain dominates and negative when relative vorticity dominates (Figure 3).

Strength of non-linear eddy interactions

To quantify the strength of non-linear eddy interactions, we here refer to the governing equations of a 1.5-layer quasi-geostrophic (QG) model on a beta plane, an idealised representation of the dynamics of ocean turbulence [64]. The dynamically conserved quantity in the QG model is quasi-geostrophic potential vorticity (QGPV),

$$q = \nabla_h^2 \psi - \frac{1}{L_R^2}\psi + \beta y, \tag{14}$$

where q is the QGPV, ψ is the streamfunction for the geostrophic flow which is calculated from the SSH,

$$\psi = \frac{g}{f}\eta, \tag{15}$$

and L_R is the Rossby deformation radius. The three contributions to QGPV on the right-hand side in Equation 14 are the relative vorticity, the effect of vortex stretching in the vertical direction, and the meridional gradient of planetary vorticity respectively and q is materially conserved by the geostrophic flow,

$$\frac{\partial q}{\partial t} + J(\psi, q) = 0, \tag{16}$$

where $J(a,b)$ is the Jacobian operator,

$$J(a,b) = \frac{\partial a}{\partial x}\frac{\partial b}{\partial y} - \frac{\partial a}{\partial y}\frac{\partial b}{\partial x}. \tag{17}$$

We define the strength, a, of non-linear eddy interactions,

$$a = J(\psi, \nabla_h^2 \psi), \tag{18}$$

to be the contribution of the non-linear advection of geostrophic relative vorticity, $\nabla_h^2 \psi$, to the QGPV tendency. This strength is proportional to a product of first- and third-order gradients of η,

$$a = \left(\frac{g}{f}\right)^2 \left[\frac{\partial \eta}{\partial x}\left(\frac{\partial^3 \eta}{\partial y \partial x^2} + \frac{\partial^3 \eta}{\partial y^3}\right) - \frac{\partial \eta}{\partial y}\left(\frac{\partial^3 \eta}{\partial x^3} + \frac{\partial^3 \eta}{\partial x \partial y^2}\right)\right], \tag{19}$$

and is thus strongly sensitive to the precise geometry and configuration of eddies. Since non-linear eddy interactions can both increase and decrease QGPV, a is distributed around zero and we take the standard deviation of a to be a metric for the strength of non-linear eddy interactions. While the QG model is an idealised representation of real-world ocean dynamics, this metric diagnoses the importance of non-linear eddy interactions in the dynamics and highlights regions of enhanced eddy activity (Extended Data Figure 3).

KE cascade: diagnosing energy transfer between scales

Energy transfers between flows of different length-scales, a characteristic property of turbulent flows, can be diagnosed using a coarse-graining analysis [5]. By applying convolutions to the Navier-Stokes equation and neglecting small contributions from molecular viscosity, a kinetic energy (KE) budget for the coarse-grained flow (i.e. the velocity after convolution with a smoothing filter) is obtained [5]

$$\frac{\partial}{\partial t}\rho_0 \frac{|\overline{\mathbf{u}}_l|^2}{2} = -\nabla \cdot \mathbf{J}_l^{\text{transport}} - \Pi_l + \overline{\rho}_l \mathbf{g} \cdot \overline{\mathbf{u}}_l + \rho_0 \overline{\mathbf{F}}_l^{\text{forcing}} \cdot \overline{\mathbf{u}}_l, \tag{20}$$

where $\bar{\cdot}_l$ represents convolution with a filter with scale diameter l, $\mathbf{J}_l^{\text{transport}}$ is the spatial transport of large-scale KE (as defined in ref [5]), ρ_0 is a reference density (here taken to be 1025kgm^{-3}), Π_l is the transfer of energy between scales by non-linear eddy interactions defined below, $\mathbf{g}$ is the acceleration due to gravity, and $\overline{\mathbf{F}}_l^{\text{forcing}}$ is any external forcing at scales above l (e.g. by winds). The third term on the right represents the conversion of potential energy into kinetic.

The existence of an upscale (or 'inverse') cascade of KE is a characteristic property of geophysical turbulence [64] that is hypothesised to play a role in setting the seasonality of mesoscale ocean eddies [7, 8]. We therefore here diagnose the transfer of KE between scales, Π_l, from surface geostrophic current maps to assess its magnitude and sign at different spatial scales, implicitly neglecting energy associated with vertical velocities (which are small at the scales considered here). We don't seek to close the energy budget in Equation 20 as this would require precise determination of the potential energy conversion and external forcing at the same resolution as the surface geostrophic current maps.

The KE cascade, Π_l, is caused by non-linear interactions between eddies and is characterised by the interplay between the large-scale strain tensor, $\overline{\mathbf{S}}_l$, and the subfilter-scale stress, $\overline{\tau}_l$, through [5]

$$\Pi_l = -\rho_0 \overline{S}_{ij} \overline{\tau}_{ji}, \tag{21}$$

where

$$\overline{S}_{ij} = \frac{1}{2}\left(\partial_i \overline{u}_j + \partial_j \overline{u}_i\right), \tag{22}$$

$$\overline{\tau}_{ij} = \overline{u_i u_j} - \overline{u}_i \overline{u}_j, \tag{23}$$

repeated indices are summed over, and the subscript l in the coarse-graining operation has been dropped when using index notation to avoid confusion between the coarse-graining length scale and a spatial index. The cascade term, Π_l, represents the energy transfer from scales larger than l to smaller scales due to non-linear eddy interactions, so Π_l is positive (negative), energy is transferred from scales larger (smaller) than l to smaller (larger) scales representing a downscale (upscale) cascade. Scrutiny of Equation 21 highlights the sensitivity of the KE cascade to the strain rate, and hence to eddy geometry.

We use an open-source code, FlowSieve [80], to coarse-grain the surface geostrophic current maps at a range of scales, l, and diagnose Π_l and $\mathbf{J}_l^{\text{transport}}$. While this coarse-graining can be done on global surface current fields accounting for the spherical geometry of the Earth's surface [80], we here restrict our attention to a selection of open ocean regions (defined in Extended Data Table 1). This prevents the need to prescribe boundary conditions at coastlines and significantly reduces the computational requirements of the analysis. All velocities are first projected onto a local ortho-normal grid with a grid spacing 10km and side length of 2560km. We perform coarse-graining on this grid and diagnose Π_l and $\mathbf{J}_l^{\text{transport}}$ as a function of l and

time at each grid point, before taking a spatial average of both quantities over a smaller box in the centre of the domain with side length 1280km. The smoothing filter used in the coarse-graining is a smoothed top-hat, as used in previous studies [81]

$$G_l(\mathbf{r}) = \frac{A}{2}\left(1 - \tanh\left[10\left(\frac{|\mathbf{r}|}{l/2} - 1\right)\right]\right), \tag{24}$$

where A is a normalisation calculated numerically to ensure G_l integrates to unity and $\mathbf{r}$ is the separation between the evaluation point and the centre of the convolutional kernel. The coarse-grained fields, $\overline{f}_l(\mathbf{x})$, are then defined as

$$\overline{f}_l(\mathbf{x}) = G_l * f, \tag{25}$$

where $*$ is a two-dimensional convolution.

There is no direct correspondence between the filter scales, l, used in coarse-graining and wavelengths in a Fourier analysis (e.g. the KE spectra in Figure 5). To aid interpretation of the coarse-graining results in comparison to the spectral analysis we used to evaluate the effective resolution of each SSH map, we empirically calculate associated effective coarse-graining scales for each SSH map (method described below).

When assessing the ability of the KE cascade to drive the summer-time peak in large-scale KE, we compare the change in large-scale KE from its winter minimum to its summer maximum to the time integrals of $(-\Pi_l)$ and $(-\nabla \cdot \mathbf{J}_l^{\text{transport}})$ over the same time period. This analysis neglects sources/sinks of energy at larger scales, energy lost from surface currents due to eddy barotropisation, and conversion of potential energy to KE but in this study we don't seek to close the large-scale KE budget, merely to demonstrate that the diagnosed Π_l is greatly changed between maps and that its strength becomes large enough to be a significant contributor to the change in large-scale KE.

Effective coarse-graining scale of SSH maps

To aid interpretation of the effective resolution metric [29], we also provide a corresponding 'effective coarse-graining scale'. This metric can be interpreted as the coarse-graining scale that best represents the smoothing induced by the SSH mapping algorithm and is useful when considering our KE cascade results which were obtained using coarse-graining.

The effective coarse-graining scale is obtained by positing that the mapped signal can reasonably be approximated as a coarsened version of the true signal where a smoothing kernel has been convolved with the observations.

For a mapped along-track signal x, and an observed signal y, the effective resolution is defined [29] as the wavelength where the function, f, crosses 0.5, where

$$f(k) = 1 - \frac{\widehat{(x-y)}^* \widehat{(x-y)}}{\hat{y}^* \hat{y}}, \tag{26}$$

where * represents complex conjugation, a "hat" is the Fourier transform, and k is the along-track wavenumber.

We suppose that the mapped signal, x, can be approximated as the convolution of y with a smoothing kernel, G_l, with corresponding spatial scale, l,

$$x = G_l * y. \tag{27}$$

Using the convolution theorem and plugging this definition of x into Equation 26 yields an expression for f in terms of the smoothing kernel

$$f(k) = \hat{G}_l + \hat{G}_l^{\,*} - \hat{G}_l^{\,*}\hat{G}_l. \tag{28}$$

For any given kernel, G_l, its Fourier transform, and hence $f(k)$, depends only on the coarse-graining scale, l. Thus for each map and region we fit the function in Equation 28 to the data for $f(k)$ for different coarse-graining kernels, G_l, to find corresponding coarse-graining scales, l. We refer to the resulting scale as the 'effective coarse-graining scale' of the SSH map for each kernel.

In Extended Data Table 4, we compare the effective resolution to the effective coarse-graining scales for a Guassian kernel

$$G_l^{\text{Gaussian}}(x - x') = \frac{1}{l\sqrt{2\pi}} \exp\left(-\frac{|x-x'|^2}{2l^2}\right), \tag{29}$$

and the smooth top-hat kernel

$$G_l^{\text{FlowSieve}}(x - x') = \frac{A}{2}\left(1 - \tanh\left[10\left(\frac{|x-x'|}{l/2} - 1\right)\right]\right), \tag{30}$$

used in FlowSieve [80] that we used to diagnose the energy transfer between scales, where $|x-x'|$ is the distance between the analysis point and the kernel centre and A is a normalisation factor computed numerically. Note that for $G_l^{\text{FlowSieve}}$ the Fourier transform becomes oscillatory at high wavenumbers, we therefore set all values of the fitted $f(k)$ to zero at wavenumbers past the first zero crossing to ensure we only fit the physically meaningful part of the curve to the data.

Data Availability

The high-resolution global SSH maps, surface currents, strain rate, and relative vorticity for 2019 created in this study are freely available here: (link to data which will be published upon acceptance). We plan in the near future to produce similar maps for other years and distribute these to the scientific community through NASA PO.DAAC as the storage requirements are too large for us to host this dataset. All satellite and surface drifter data used in this study are publicly available for download and the specific datasets are referenced in the text. The Ocean Data Challenge mapping inter-comparison framework for the global SSH maps (https://github.com/ocean-data-challenges/2023a_SSH_mapping_OSE) and for the Gulf Stream Extension regional experiment (https://github.com/ocean-data-challenges/2021a_SSH_mapping_OSE) are both freely available on GitHub and provide instructions for how to access the data for other SSH mapping methods. The Gulf Stream SSH maps for Febvre et al. 2023 [40] and Archambault et al. 2023 [39] are available at https://doi.org/10.5281/zenodo.8064113 and https://gitlab.lip6.fr/archambault/visapp2023 respectively.

Code Availability

The python code for reproducing our SSH mapping is available here: https://github.com/smartin98/Global_DL_SSH. The coarse-graining code used in this study, FlowSieve [80], is available here: https://github.com/husseinaluie/FlowSieve.

References

1. Wunsch, C. Where do ocean eddy heat fluxes matter? *J. Geophys. Res. Ocean.* **104**, 13235–13249 (1999).
2. Jayne, S. R. & Marotzke, J. The oceanic eddy heat transport. *J. Phys. Oceanogr.* **32**, 3328–3345 (2002).
3. Zhang, Z., Wang, W. & Qiu, B. Oceanic mass transport by mesoscale eddies. *Sci.* **345**, 322–324 (2014).
4. Ferrari, R. & Wunsch, C. Ocean circulation kinetic energy: Reservoirs, sources, and sinks. *Annu. Rev. Fluid Mech.* **41**, 253–282 (2009).
5. Aluie, H., Hecht, M. & Vallis, G. K. Mapping the energy cascade in the north atlantic ocean: The coarse-graining approach. *J. Phys. Oceanogr.* **48**, 225–244 (2018).
6. Klein, P. *et al.* Ocean-scale interactions from space. *Earth Space Sci.* **6**, 795–817 (2019).
7. Sasaki, H., Klein, P., Qiu, B. & Sasai, Y. Impact of oceanic-scale interactions on the seasonal modulation of ocean dynamics by the atmosphere. *Nat. communications* **5**, 5636 (2014).
8. Qiu, B., Chen, S., Klein, P., Sasaki, H. & Sasai, Y. Seasonal mesoscale and submesoscale eddy variability along the north pacific subtropical countercurrent. *J. Phys. Oceanogr.* **44**, 3079–3098 (2014).
9. Uchida, T., Abernathey, R. & Smith, S. Seasonality of eddy kinetic energy in an eddy permitting global climate model. *Ocean. Model.* **118**, 41–58 (2017).
10. Schubert, R., Gula, J., Greatbatch, R. J., Baschek, B. & Biastoch, A. The submesoscale kinetic energy cascade: Mesoscale absorption of submesoscale mixed layer eddies and frontal downscale fluxes. *J. Phys. Oceanogr.* **50**, 2573–2589 (2020).
11. Ajayi, A. *et al.* Diagnosing cross-scale kinetic energy exchanges from two submesoscale permitting ocean models. *J. Adv. Model. Earth Syst.* **13**, e2019MS001923 (2021).
12. Balwada, D., Xie, J.-H., Marino, R. & Feraco, F. Direct observational evidence of an oceanic dual kinetic energy cascade and its seasonality. *Sci. Adv.* **8**, eabq2566 (2022).
13. Garabato, A. C. N. *et al.* Kinetic energy transfers between mesoscale and submesoscale motions in the open ocean's upper layers. *J. Phys. Oceanogr.* **52**, 75–97 (2022).
14. Steinberg, J. M., Cole, S. T., Drushka, K. & Abernathey, R. P. Seasonality of the mesoscale inverse cascade as inferred from global scale-dependent eddy energy observations. *J. Phys. Oceanogr.* **52**, 1677–1691 (2022).
15. Lawrence, A. & Callies, J. Seasonality and spatial dependence of mesoscale and submesoscale ocean currents from along-track satellite altimetry. *J. Phys. Oceanogr.* **52**, 2069–2089 (2022).
16. Schubert, R., Vergara, O. & Gula, J. The open ocean kinetic energy cascade is strongest in late winter and spring. *Commun. Earth & Environ.* **4**, 450 (2023).
17. Storer, B. A., Buzzicotti, M., Khatri, H., Griffies, S. M. & Aluie, H. Global cascade of kinetic energy in the ocean and the atmospheric imprint. *arXiv preprint arXiv:2311.09100* (2023).
18. Callies, J., Ferrari, R., Klymak, J. M. & Gula, J. Seasonality in submesoscale turbulence. *Nat. communications* **6**, 6862 (2015).
19. Buckingham, C. E. *et al.* Seasonality of submesoscale flows in the ocean surface boundary layer. *Geophys. Res. Lett.* **43**, 2118–2126 (2016).
20. Taylor, J. R. & Thompson, A. F. Submesoscale dynamics in the upper ocean. *Annu. Rev. Fluid Mech.* **55**, 103–127 (2023).
21. Hoskins, B. J. The mathematical theory of frontogenesis. *Annu. review fluid mechanics* **14**, 131–151 (1982).

22. Siegelman, L. *et al.* Enhanced upward heat transport at deep submesoscale ocean fronts. *Nat. Geosci.* **13**, 50–55 (2020).

23. Mahadevan, A. The impact of submesoscale physics on primary productivity of plankton. *Annu. review marine science* **8**, 161–184 (2016).

24. Gent, P. R. & Mcwilliams, J. C. Isopycnal mixing in ocean circulation models. *J. Phys. Oceanogr.* **20**, 150–155 (1990).

25. Hewitt, H. T. *et al.* Resolving and parameterising the ocean mesoscale in earth system models. *Curr. Clim. Chang. Reports* **6**, 137–152 (2020).

26. Chelton, D. B., Schlax, M. G. & Samelson, R. M. Global observations of nonlinear mesoscale eddies. *Prog. oceanography* **91**, 167–216 (2011).

27. Dufau, C., Orsztynowicz, M., Dibarboure, G., Morrow, R. & Le Traon, P.-Y. Mesoscale resolution capability of altimetry: Present and future. *J. Geophys. Res. Ocean.* **121**, 4910–4927 (2016).

28. Taburet, G. *et al.* DUACS DT2018: 25 years of reprocessed sea level altimetry products. *Ocean. Sci.* **15**, 1207–1224 (2019).

29. Ballarotta, M. *et al.* On the resolutions of ocean altimetry maps. *Ocean. Sci.* **15**, 1091–1109 (2019).

30. Ubelmann, C., Klein, P. & Fu, L.-L. Dynamic interpolation of sea surface height and potential applications for future high-resolution altimetry mapping. *J. Atmospheric Ocean. Technol.* **32**, 177–184 (2015).

31. Ubelmann, C. *et al.* Reconstructing ocean surface current combining altimetry and future spaceborne doppler data. *J. Geophys. Res. Ocean.* **126**, e2020JC016560 (2021).

32. Le Guillou, F. *et al.* Mapping altimetry in the forthcoming swot era by back-and-forth nudging a one-layer quasigeostrophic model. *J. Atmospheric Ocean. Technol.* **38**, 697–710 (2021).

33. Metref, S. *et al.* Ocean data challenges (2023). https://ocean-data-challenges.github.io/.

34. Manucharyan, G. E., Siegelman, L. & Klein, P. A deep learning approach to spatiotemporal sea surface height interpolation and estimation of deep currents in geostrophic ocean turbulence. *J. Adv. Model. Earth Syst.* **13**, e2019MS001965 (2021).

35. Fablet, R., Amar, M. M., Febvre, Q., Beauchamp, M. & Chapron, B. End-to-end physics-informed representation learning for satellite ocean remote sensing data: Applications to satellite altimetry and sea surface currents. *ISPRS Annals Photogramm. Remote. Sens. & Spatial Inf. Sci.* (2021).

36. Beauchamp, M., Febvre, Q., Georgenthum, H. & Fablet, R. 4dvarnet-ssh: end-to-end learning of variational interpolation schemes for nadir and wide-swath satellite altimetry. *Geosci. Model. Dev. Discuss.* **2022**, 1–37 (2022).

37. Fablet, R., Febvre, Q. & Chapron, B. Multimodal 4dvarnets for the reconstruction of sea surface dynamics from sst-ssh synergies. *IEEE Transactions on Geosci. Remote. Sens.* (2023).

38. Martin, S. A., Manucharyan, G. E. & Klein, P. Synthesizing sea surface temperature and satellite altimetry observations using deep learning improves the accuracy and resolution of gridded sea surface height anomalies. *J. Adv. Model. Earth Syst.* **15**, e2022MS003589 (2023).

39. Archambault, T., Filoche, A., Charantonnis, A. & Béréziat, D. Multimodal unsupervised spatio-temporal interpolation of satellite ocean altimetry maps. In *VISAPP* (2023).

40. Febvre, Q., Sommer, J. L., Ubelmann, C. & Fablet, R. Training neural mapping schemes for satellite altimetry with simulation data. *arXiv preprint arXiv:2309.14350* (2023).

41. LeCun, Y., Bengio, Y. & Hinton, G. Deep learning. *nature* **521**, 436–444 (2015).

42. Schneider, T., Lan, S., Stuart, A. & Teixeira, J. Earth system modeling 2.0: A blueprint for models that learn from observations and targeted high-resolution simulations. *Geophys. Res. Lett.* **44**, 12–396 (2017).

43. Weyn, J. A., Durran, D. R., Caruana, R. & Cresswell-Clay, N. Sub-seasonal forecasting with a large ensemble of deep-learning weather prediction models. *J. Adv. Model. Earth Syst.* **13**, e2021MS002502 (2021).

44. Pathak, J. *et al.* Fourcastnet: A global data-driven high-resolution weather model using adaptive fourier neural operators. *arXiv preprint arXiv:2202.11214* (2022).

45. Lam, R. *et al.* Learning skillful medium-range global weather forecasting. *Sci.* eadi2336 (2023).

46. George, T. M., Manucharyan, G. E. & Thompson, A. F. Deep learning to infer eddy heat fluxes from sea surface height patterns of mesoscale turbulence. *Nat. communications* **12**, 800 (2021).

47. Goh, E., Yepremyan, A. R., Wang, J. & Wilson, B. Maesstro: Masked autoencoders for sea surface temperature reconstruction under occlusion. *EGUsphere* **2023**, 1–20 (2023).

48. Agabin, A., Prochaska, J. X., Cornillon, P. C. & Buckingham, C. E. Mitigating masked pixels in climate-critical datasets. *arXiv preprint arXiv:2307.09227* (2023).

49. Isern-Fontanet, J., Chapron, B., Lapeyre, G. & Klein, P. Potential use of microwave sea surface temperatures for the estimation of ocean currents. *Geophys. research letters* **33** (2006).

50. Ubelmann, C. *et al.* Simultaneous estimation of ocean mesoscale and coherent internal tide sea surface height signatures from the global altimetry record. *Ocean. Sci.* **18**, 469–481 (2022).

51. Ballarotta, M. *et al.* Improved global sea surface height and current maps from remote sensing and in situ observations.

Earth Syst. Sci. Data **15**, 295–315 (2023).

52. Cornillon, P. C. *et al.* Oceans. In Galperin, B. & Read, P. (eds.) *Zonal Jets Phenomenology, Genesis, and Physics*, chap. 3, 46 – 71 (Cambridge University Press, 2019). DOI 10.1017/9781107358225.003.

53. Ballarotta, M. *et al.* Ocean data challenges (2021). https://github.com/ocean-data-challenges/2021a_SSH_mapping_OSE.

54. Le Traon, P., Nadal, F. & Ducet, N. An improved mapping method of multisatellite altimeter data. *J. atmospheric oceanic technology* **15**, 522–534 (1998).

55. Scott, R. B. & Wang, F. Direct evidence of an oceanic inverse kinetic energy cascade from satellite altimetry. *J. Phys. Oceanogr.* **35**, 1650–1666 (2005).

56. Capet, X., McWilliams, J. C., Molemaker, M. J. & Shchepetkin, A. F. Mesoscale to submesoscale transition in the california current system. part iii: Energy balance and flux. *J. Phys. Oceanogr.* **38**, 2256–2269 (2008).

57. Morrow, R. *et al.* Global observations of fine-scale ocean surface topography with the surface water and ocean topography (swot) mission. *Front. Mar. Sci.* **6**, 232 (2019).

58. Zhang, C. *et al.* Implementation and evaluation of a machine learned mesoscale eddy parameterization into a numerical ocean circulation model. *J. Adv. Model. Earth Syst.* **15**, e2023MS003697 (2023).

59. Siegelman, L., Klein, P., Thompson, A. F., Torres, H. S. & Menemenlis, D. Altimetry-based diagnosis of deep-reaching sub-mesoscale ocean fronts. *Fluids* **5**, 145 (2020).

60. Gaultier, L., Ubelmann, C. & Fu, L.-L. The challenge of using future swot data for oceanic field reconstruction. *J. Atmospheric Ocean. Technol.* **33**, 119–126 (2016).

61. Febvre, Q., Fablet, R., Le Sommer, J. & Ubelmann, C. Joint calibration and mapping of satellite altimetry data using trainable variational models. In *ICASSP 2022-2022 IEEE International Conference on Acoustics, Speech and Signal Processing (ICASSP)*, 1536–1540 (IEEE, 2022).

62. Dosovitskiy, A. *et al.* An image is worth 16x16 words: Transformers for image recognition at scale. *arXiv preprint arXiv:2010.11929* (2020).

63. Nguyen, T., Brandstetter, J., Kapoor, A., Gupta, J. K. & Grover, A. Climax: A foundation model for weather and climate. *arXiv preprint arXiv:2301.10343* (2023).

64. Vallis, G. K. *Atmospheric and oceanic fluid dynamics* (Cambridge University Press, 2017).

65. E.U. Copernicus Marine Service Information (CMEMS). Global ocean along track l 3 sea surface heights reprocessed 1993 ongoing tailored for data assimilation (2023). URL https://doi.org/10.48670/moi-00146. Accessed on 04-09-2023.

66. E.U. Copernicus Marine Service Information (CMEMS). Global ocean along track l 3 sea surface heights nrt (2023). URL https://doi.org/10.48670/moi-00147. Accessed on 04-09-2023.

67. JPL MUR MEaSUREs Project. Ghrsst level 4 mur global foundation sea surface temperature analysis. ver. 4.1 (2015). URL https://doi.org/10.5067/GHGMR-4FJ04. Accessed on 04-09-2023.

68. Chin, T. M., Vazquez-Cuervo, J. & Armstrong, E. M. A multi-scale high-resolution analysis of global sea surface temperature. *Remote. sensing environment* **200**, 154–169 (2017).

69. Srivastava, N., Mansimov, E. & Salakhudinov, R. Unsupervised learning of video representations using lstms. In *International conference on machine learning*, 843–852 (PMLR, 2015).

70. Gao, Z., Tan, C., Wu, L. & Li, S. Z. Simvp: Simpler yet better video prediction. In *Proceedings of the IEEE/CVF Conference on Computer Vision and Pattern Recognition (CVPR)*, 3170–3180 (2022).

71. Tan, C., Gao, Z., Li, S. & Li, S. Z. Simvp: Towards simple yet powerful spatiotemporal predictive learning. *arXiv preprint arXiv:2211.12509* (2022).

72. Shi, X. *et al.* Convolutional lstm network: A machine learning approach for precipitation nowcasting. *Adv. neural information processing systems* **28** (2015).

73. Callaham, J. L., Maeda, K. & Brunton, S. L. Robust flow reconstruction from limited measurements via sparse representation. *Phys. Rev. Fluids* **4**, 103907 (2019).

74. Arbic, B. K., Scott, R. B., Chelton, D. B., Richman, J. G. & Shriver, J. F. Effects of stencil width on surface ocean geostrophic velocity and vorticity estimation from gridded satellite altimeter data. *J. Geophys. Res. Ocean.* **117** (2012).

75. Metref, S. & Ballarotta, M. Ocean data challenges (2023). https://github.com/ocean-data-challenges/2023a_SSH_mapping_OSE.

76. E.U. Copernicus Marine Service Information (CMEMS). Global ocean-delayed mode in situ observations of surface (drifters, hfr) and sub-surface (vessel-mounted adcps) water velocity (2023). URL https://doi.org/10.17882/86236. Accessed on 04-09-2023.

77. Bretherton, F. P., Davis, R. E. & Fandry, C. A technique for objective analysis and design of oceanographic experiments applied to mode-73. In *Deep Sea Research and Oceanographic Abstracts*, vol. 23, 559–582 (Elsevier, 1976).

78. Okubo, A. Horizontal dispersion of floatable particles in the vicinity of velocity singularities such as convergences. In *Deep sea research and oceanographic abstracts*, vol. 17, 445–454 (Elsevier, 1970).
79. Weiss, J. The dynamics of enstrophy transfer in two-dimensional hydrodynamics. *Phys. D: Nonlinear Phenom.* **48**, 273–294 (1991).
80. Storer, B. A. & Aluie, H. Flowsieve: A coarse-graining utility for geophysical flows on the sphere. *J. Open Source Softw.* **8**, 4277 (2023).
81. Storer, B. A., Buzzicotti, M., Khatri, H., Griffies, S. M. & Aluie, H. Global energy spectrum of the general oceanic circulation. *Nat. communications* **13**, 5314 (2022).

Acknowledgements

The research was funded by the National Aeronautics and Space Administration under Grant 80NSSC21K1187 issued through the Science Mission Directorate, Ocean Surface Topography Science Team program. S.A.M. received further financial support from the Theodore H. and Marie M. Sarchin Endowed Fellowship in Oceanography. P.K. acknowledges support from the SWOT Science Team and the QuikSCAT mission. The authors acknowledge helpful discussions with Steven Brunton, Jinbo Wang, Brian Arbic, Quentin Febvre, Tom Farrar, J. Xavier Prochaska, Peter Cornillon, and Christian Buckingham and thank all those involved in creating and maintaining the Ocean Data Challenges, especially Sammy Metref and Maxime Ballarotta. Computational resources supporting this work were provided by the NASA High-End Computing (HEC) Program through the NASA Advanced Supercomputing (NAS) Division at Ames Research Center. S.A.M. and G.E.M. thank David Darr for maintaining computational resources at the University of Washington. G.E.M. thanks Charles Trimble for funding conceptual studies of deep learning methods for SSH mapping at the California Institute of Technology.

Author contributions statement

S.A.M.: study conceptualisation, code writing, data analysis, interpretation of results, writing and editing of the manuscript. G.E.M. & P.K.: study conceptualisation, interpretation of results, writing and editing of the manuscript.

Competing interests

The authors declare no competing interests.

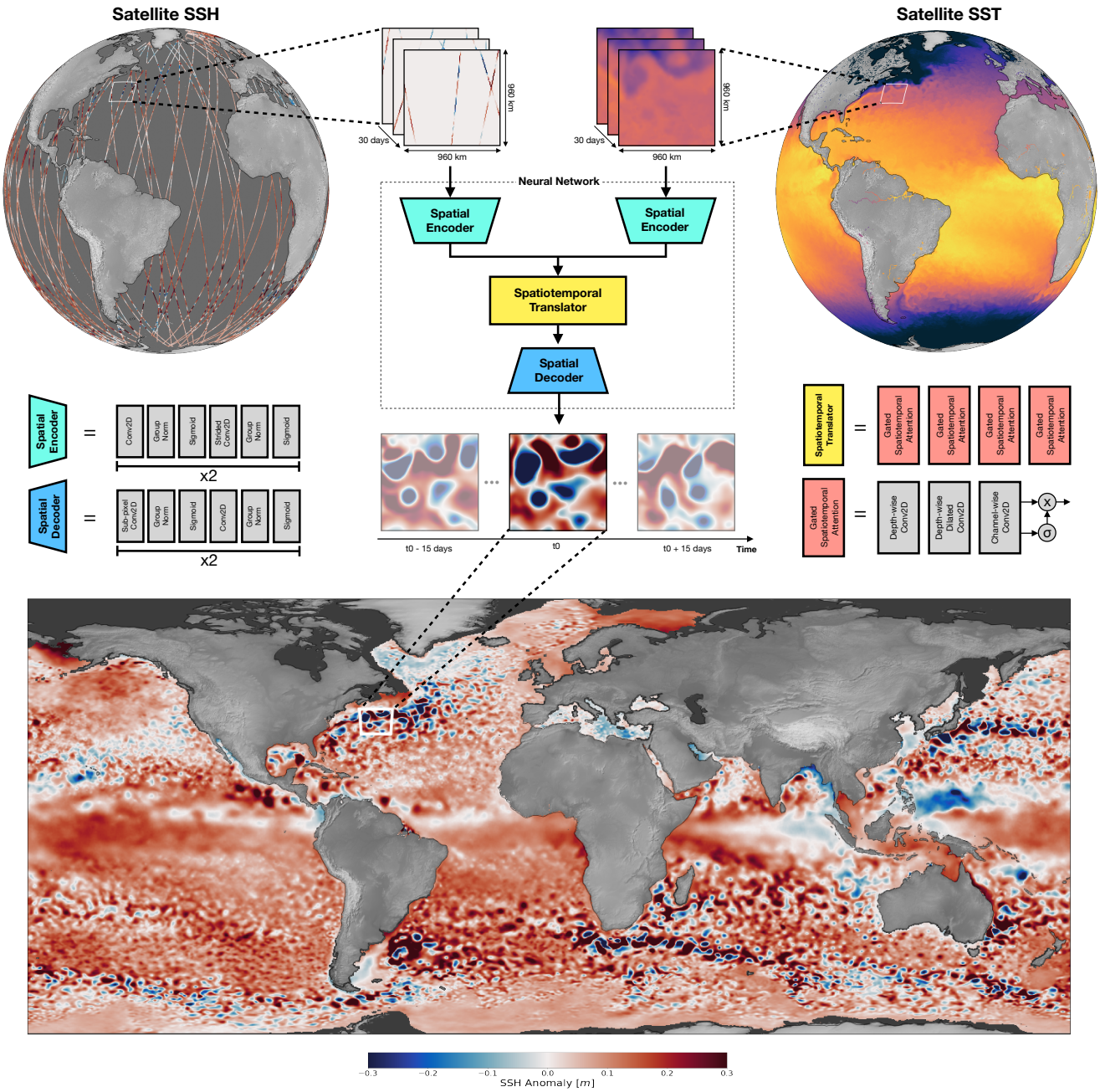

Figure 1. Schematic of our deep learning method for mapping SSH from satellite altimetry and SST observations.

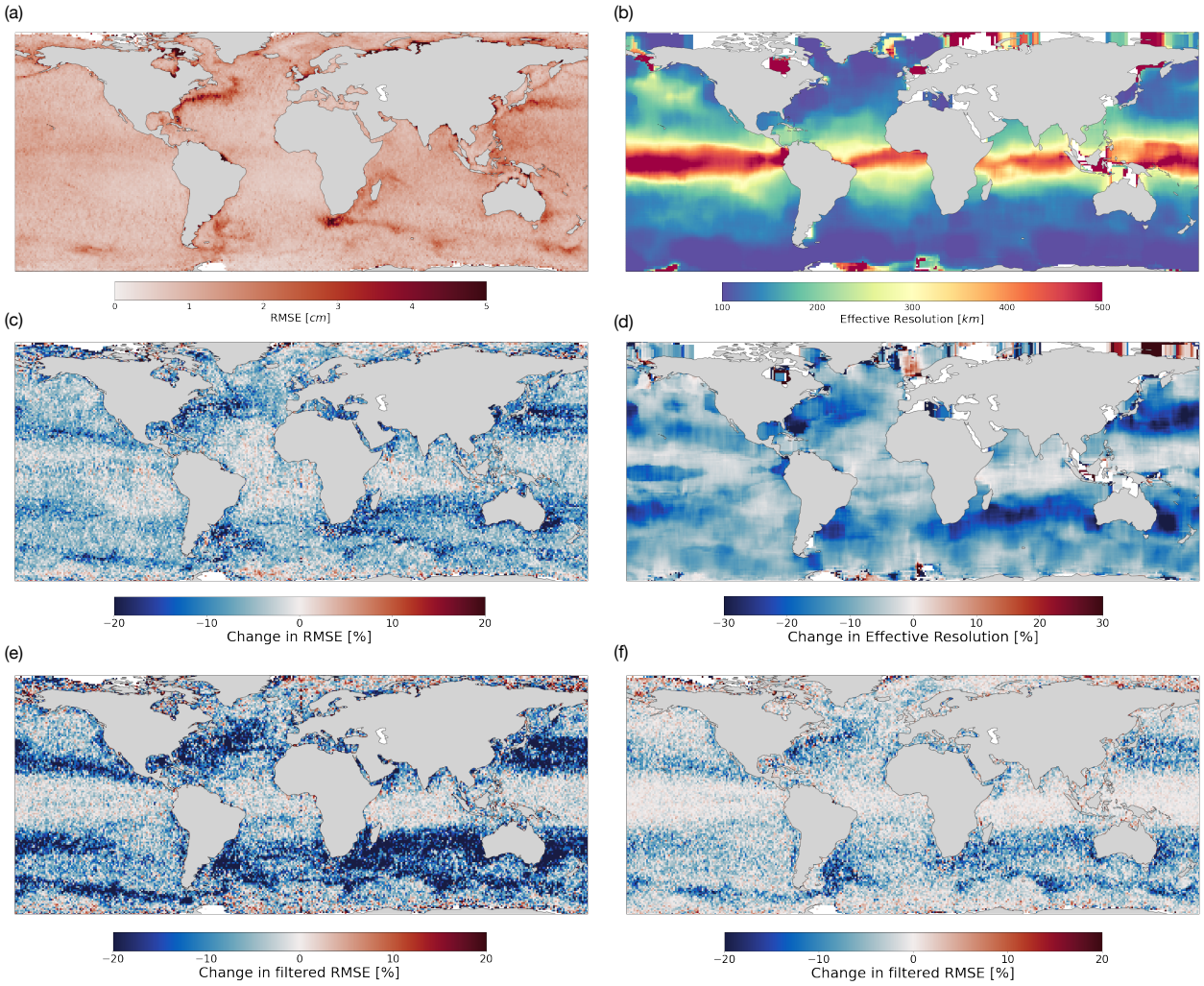

Figure 2. Evaluation of deep learning SSH maps against withheld satellite altimeter observations. (a) root-mean-square error (RMSE) of SimVP SSH-SST. (b) Smallest resolved wavelengths (effective resolution) of SimVP SSH-SST. (c) Change in RMSE of SimVP SSH-SST compared to DUACS. (d) Change in effective resolution of SimVP SSH-SST compared to DUACS. (e) Change in RMSE of small-scale (70-250km) signals of SimVP SSH-SST compared to DUACS. (f) Change in RMSE of small-scale (70-250km wavelength) signals of SimVP SSH-SST compared to SimVP SSH (which does not use SST).

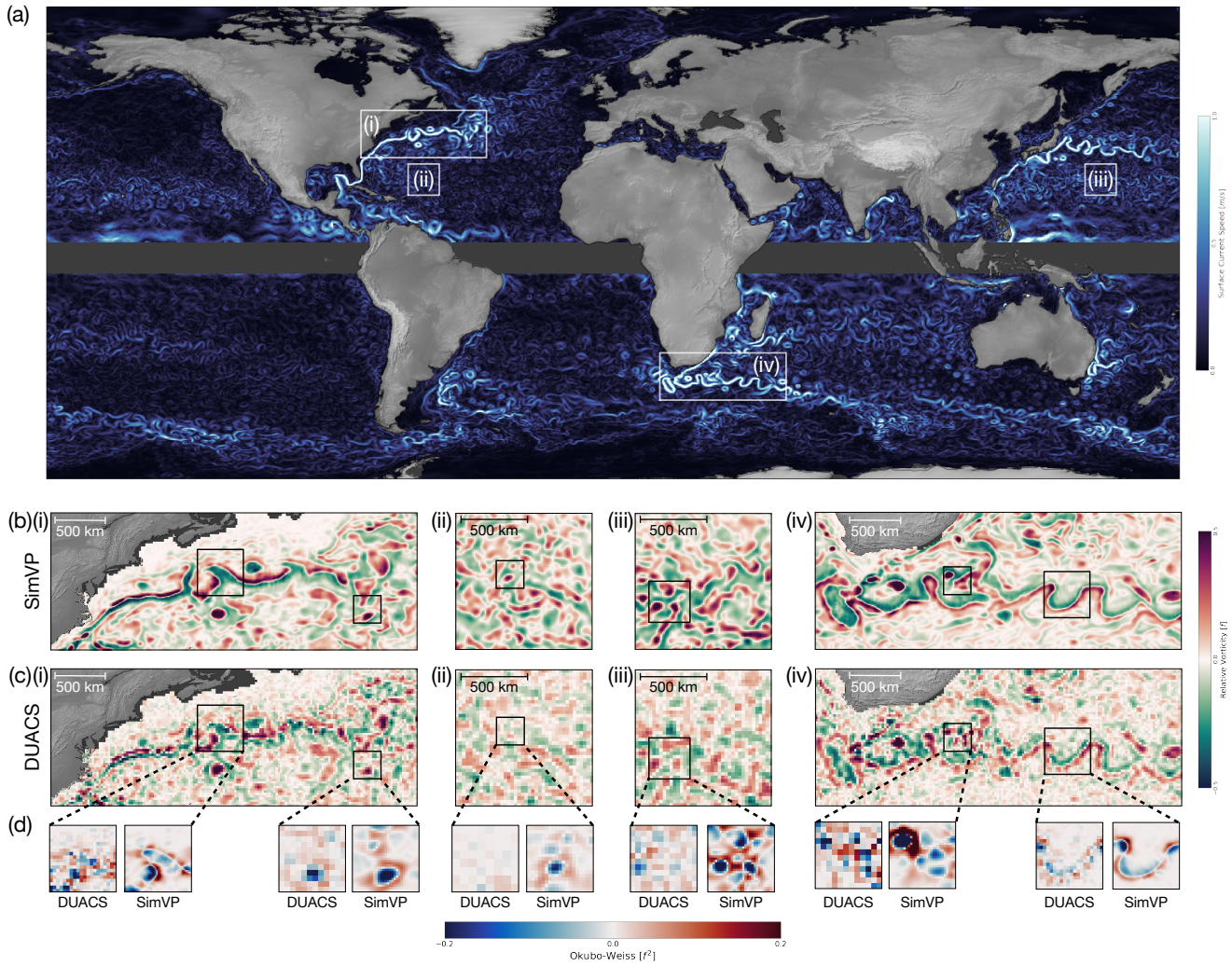

Figure 3. Visual comparison of surface currents from deep learning (SimVP SSH-SST) and linear optimal interpolation (DUACS). (a) Surface geostrophic current speed on March 1st 2019 derived from SSH maps made using SimVP SSH-SST. (b) Relative vorticity (normalised by local Coriolis frequency) for the SimVP SSH-SST surface currents. (c) Relative vorticity for the DUACS surface currents. (d) Zoomed insets show the Okubo-Weiss quantity for both DUACS and SimVP SSH-SST.

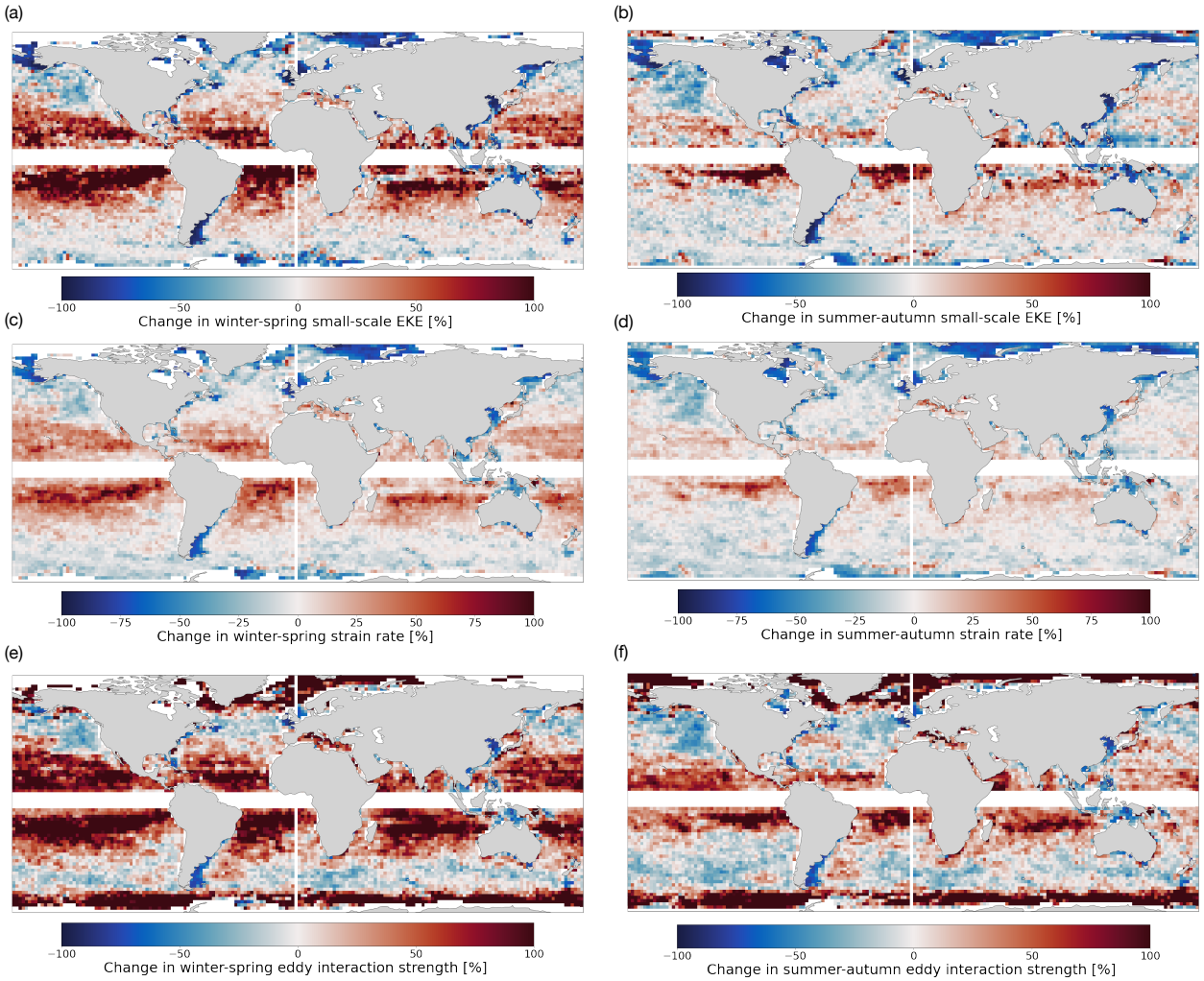

Figure 4. Changes in diagnostics of eddy energy and dynamics from SimVP SSH-SST currents compared to DUACS. (a) Winter-spring mean EKE for flows with wavelength below 250km. (b) Same as (a) but averaged over summer and autumn. (c) Winter-spring mean strain rate. (d) same as (c) but averaged over summer and autumn. (e) Winter-spring mean of strength of non-linear eddy interactions. (f) Same as (e) but averaged over summer and autumn. Absolute values of these quantities are shown in Figure 3.

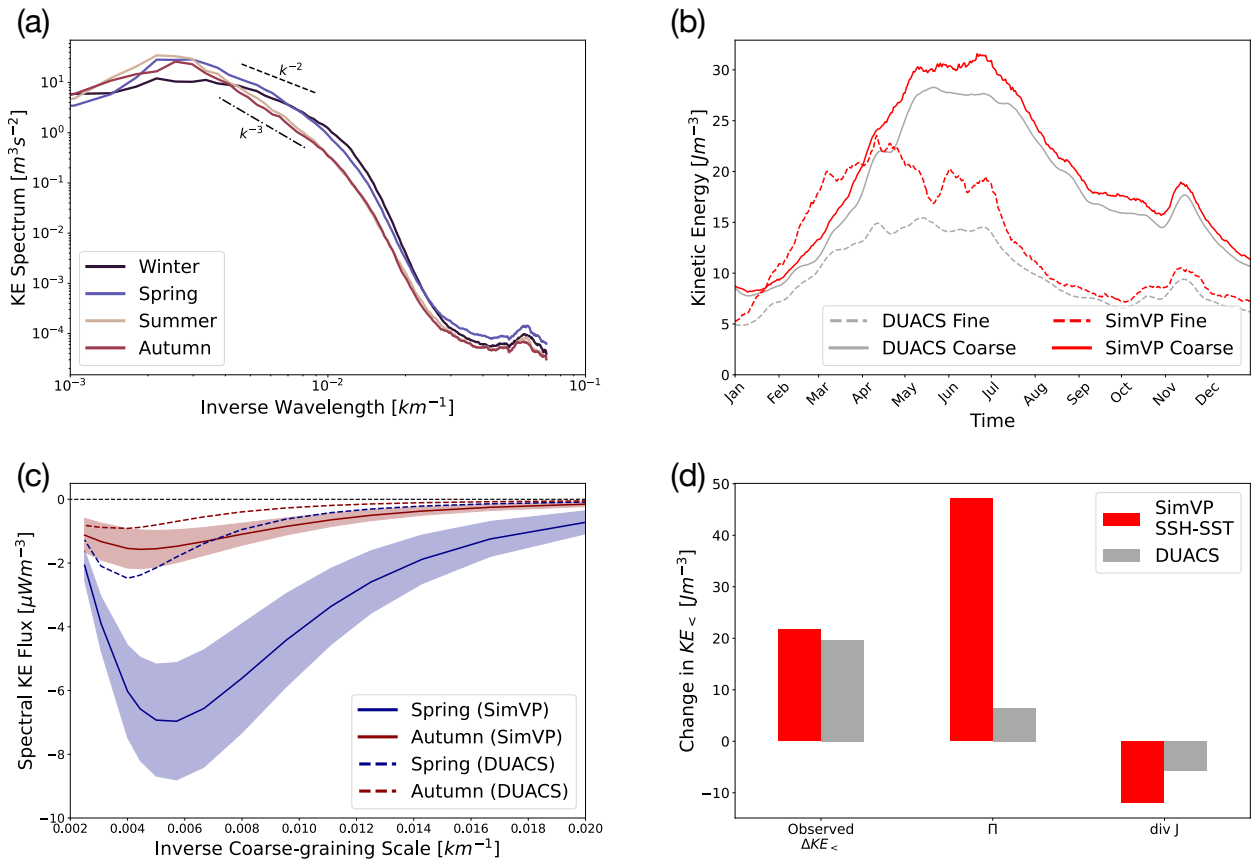

Figure 5. Upscale energy cascade revealed to be a key driver of the mesoscale KE peak in the North Pacific Subtropical Countercurrent. (a) KE spectra from SimVP surface current maps split by season. (b) Time-series of coarse- and fine-scale KE (above and below coarse-graining scale of 125km respectively) from SimVP SSH-SST (red) and DUACS (grey). (c) KE cascade as a function of coarse-graining scale from SimVP SSH-SST maps for the seasons of maximum (Spring) and minimum (Autumn) upscale cascade. Solid lines and shading are the mean and standard deviation respectively for SimVP SSH-SST, dashed lines are the mean cascades estimated from DUACS. (d) Change in coarse-scale KE ($KE_<$) from the winter-time minimum to the summer-time maximum compared to the diagnosed contribution of the spectral flux ($-\int \Pi dt$), and the diagnosed contribution of spatial transport of coarse-scale KE ($-\int \nabla \cdot J dt$) for SimVP (red) and DUACS (grey).

Extended Data

Extended Data Table 1. RMSE, filtered RMSE (signals between 70-250km), and effective resolution of the existing global SSH products compared to our deep learning method with and without SST in a selection of regions [75]. We show only the variant of the MIOST method that gives the best RMSE in each region. Bold values indicate the best-performing method on each metric.

Region	Mapping Method	RMSE [cm]	RMSE (70-250km) [cm]	Effective Resolution [km]
Gulf Stream (295-305°E, 33-43°N)	DUACS	5.66	2.44	126
	MIOST (geos)	5.61	2.41	120
	SimVP SSH	5.33	2.29	114
	SimVP SSH-SST	**5.01**	**2.19**	**107**
N Atlantic (322-338°E, 39-51°N)	DUACS	4.15	1.33	133
	MIOST (geos + waves)	3.86	1.25	129
	SimVP SSH	3.85	1.19	121
	SimVP SSH-SST	**3.78**	**1.12**	**116**
Mediterranean (2-19°E, 31-44°N)	DUACS	4.24	1.02	150
	MIOST (geos + waves)	3.97	0.97	128
	SimVP SSH	3.95	0.98	112
	SimVP SSH-SST	**3.90**	**0.94**	**112**
Kuroshio (153-167°E, 29-41°N)	DUACS	5.03	2.00	163
	MIOST (geos + waves)	4.68	1.80	150
	SimVP SSH	4.52	1.69	138
	SimVP SSH-SST	**4.34**	**1.57**	**128**
Subtropical N Pacific (149-161°E, 19-31°N)	DUACS	3.79	1.47	197
	MIOST (geos + waves)	3.70	1.39	185
	SimVP SSH	3.51	1.29	171
	SimVP SSH-SST	**3.42**	**1.22**	**156**
Equatorial Pacific (175-250°E, 10°S-10°N)	DUACS	3.30	1.11	490
	MIOST (geos + waves)	3.21	1.10	**445**
	SimVP SSH	3.21	1.10	456
	SimVP SSH-SST	**3.19**	**1.09**	448
Brazil-Malvinas (305-325°E, 40-55°S)	DUACS	4.55	1.74	121
	MIOST (geos)	4.45	1.74	118
	SimVP SSH	4.38	1.67	113
	SimVP SSH-SST	**4.09**	**1.47**	**103**
Agulhas (10-30°E, 35-45°S)	DUACS	6.09	2.55	144
	MIOST (geos + waves)	6.05	2.52	141
	SimVP SSH	5.78	2.35	127
	SimVP SSH-SST	**5.54**	**2.19**	**118**
Subtropical S Pacific (194-206°E, 19-31°S)	DUACS	3.25	1.11	186
	MIOST (geos + waves)	3.10	1.06	174
	SimVP SSH	3.05	0.99	162
	SimVP SSH-SST	**2.97**	**0.93**	**148**
Drake Passage (290-300°E, 55-65°S)	DUACS	4.49	1.60	115
	MIOST (geos + waves)	4.44	1.62	110
	SimVP SSH	4.27	1.53	108
	SimVP SSH-SST	**4.14**	**1.44**	**97**

Extended Data Table 2. Evaluation of DUACS and SimVP SSH-SST maps generated using the stable constellation of 2 satellite altimeters operational since 1993 and used in climate studies. The metrics are as in Extended Data Table 1. Bold values indicate the best performing method on each metric. Numbers in brackets give metrics for the 6 altimeter constellation (as in Extended Data Table 1).

Region	Mapping Method	RMSE [cm]	RMSE (70-250km) [cm]	Effective Resolution [km]
Gulf Stream	DUACS	7.50 (5.66)	3.48 (2.44)	159 (126)
	SimVP SSH-SST	**5.58** (5.01)	**2.39** (2.19)	**115** (107)
N Atlantic	DUACS	4.64 (4.15)	1.64 (1.33)	153 (133)
	SimVP SSH-SST	**3.92** (3.78)	**1.23** (1.12)	**122** (116)
Mediterranean	DUACS	4.49 (4.24)	1.27 (1.02)	250 (150)
	SimVP SSH-SST	**4.01** (3.90)	**1.06** (0.94)	**144** (112)
Kuroshio	DUACS	6.16 (5.03)	2.65 (2.00)	197 (163)
	SimVP SSH-SST	**4.65** (4.34)	**1.77** (1.57)	**139** (128)
Subtropical N Pacific	DUACS	4.21 (3.79)	1.74 (1.47)	227 (197)
	SimVP SSH-SST	**3.54** (3.42)	**1.31** (1.22)	**169** (156)
Equatorial Pacific	DUACS	3.40 (3.30)	1.14 (1.11)	566 (490)
	SimVP SSH-SST	**3.25** (3.19)	**1.10** (1.09)	**472** (448)
Brazil-Malvinas	DUACS	5.98 (4.55)	2.55 (1.74)	152 (121)
	SimVP SSH-SST	**4.50** (4.09)	**1.74** (1.47)	**110** (103)
Agulhas	DUACS	7.85 (6.09)	3.53 (2.55)	176 (144)
	SimVP SSH-SST	**6.05** (5.54)	**2.50** (2.19)	**128** (118)
Subtropical S Pacific	DUACS	3.51 (3.25)	1.27 (1.11)	206 (186)
	SimVP SSH-SST	**3.03** (2.97)	**0.97** (0.93)	**155** (148)
Drake Passage	DUACS	4.98 (4.49)	1.96 (1.60)	131 (115)
	SimVP SSH-SST	**4.31** (4.14)	**1.56** (1.44)	**108** (97)

Extended Data Table 3. RMSE and effective resolution of published SSH mapping methods in the Gulf Stream [53]. Bold values indicate the best-performing method on each metric. Note that the results for ConvLSTM shown here differ from those published in our previous work [38] as the maps used here were created by merging multiple patch reconstructions together (as described in Methods), however, the network and weights used are the same as in our previous study.

Mapping Method	RMSE [cm]	Effective Resolution [km]
DUACS [28]	7.82	152
MIOST (geos) [31]	6.93	140
DYMOST [30]	6.75	129
BFN-QG [32]	7.69	122
4DVarNet SSH (2022) [36]	6.63	110
4DVarNet SSH (2023) [40]	**6.00**	**100**
MUSTI [39]	6.40	115
ConvLSTM SSH [38]	6.46	114
ConvLSTM SSH-SST [38]	6.00	100
SimVP SSH-SST (global)	6.18	114
SimVP SSH-SST (fine-tuned)	6.04	108

Extended Data Table 4. Effective resolution and effective coarse-graining scales for both a standard Gaussian kernel, G_l^{Gaussian}, and the smooth top-hat kernel used in FlowSieve, $G_l^{\text{FlowSieve}}$, as defined in Methods. Bold values indicate best performing method on each metric. Effective coarse-graining scales for $G_l^{\text{FlowSieve}}$ are not given for the Mediterranean and the Equatorial Pacific since this kernel did not provide a good fit for the observed signal-to-noise ratio (Methods) in these regions.

Region	Mapping Method	Eff. Res. [km]	Eff. Scale (G_l^{Gaussian}) [km]	Eff. Scale ($G_l^{\text{FlowSieve}}$) [km]
Gulf Stream	DUACS	126	31.3	90.5
	MIOST (geos)	120	29.5	84.6
	SimVP SSH	114	28.1	79.5
	SimVP SSH-SST	**107**	**26.5**	**76.7**
N Atlantic	DUACS	133	33.4	95.7
	MIOST (geos + waves)	129	31.8	92.2
	SimVP SSH	121	30.1	86.1
	SimVP SSH-SST	**116**	**28.5**	**83.0**
Mediterranean	DUACS	150	32.7	-
	MIOST (geos + waves)	128	**28.3**	-
	SimVP SSH	112	30.9	-
	SimVP SSH-SST	**112**	30.9	-
Kuroshio	DUACS	163	40.1	115.7
	MIOST (geos + waves)	150	36.6	104.9
	SimVP SSH	138	34.3	99.8
	SimVP SSH-SST	**128**	**31.8**	**92.4**
Subtropical N Pacific	DUACS	197	45.9	132.3
	MIOST (geos + waves)	185	42.8	120.5
	SimVP SSH	171	39.4	109.4
	SimVP SSH-SST	**156**	**36.1**	**103.8**
Equatorial Pacific	DUACS	490	108.1	-
	MIOST (geos + waves)	**445**	104.2	-
	SimVP SSH	456	103.3	-
	SimVP SSH-SST	448	**101.6**	-
Brazil-Malvinas	DUACS	121	29.8	85.1
	MIOST (geos)	118	29.3	84.3
	SimVP SSH	113	28.0	79.6
	SimVP SSH-SST	**103**	**25.7**	**73.5**
Agulhas	DUACS	144	36.4	104.3
	MIOST (geos + waves)	141	35.0	102.3
	SimVP SSH	127	31.4	91.7
	SimVP SSH-SST	**118**	**29.2**	**84.9**
Subtropical S Pacific	DUACS	186	45.8	132.5
	MIOST (geos + waves)	174	42.7	120.7
	SimVP SSH	162	39.2	109.7
	SimVP SSH-SST	**148**	**35.7**	**103.4**
Drake Passage	DUACS	115	28.8	80.8
	MIOST (geos + waves)	110	27.5	78.0
	SimVP SSH	108	27.2	77.7
	SimVP SSH-SST	**97**	**25.4**	**72.7**

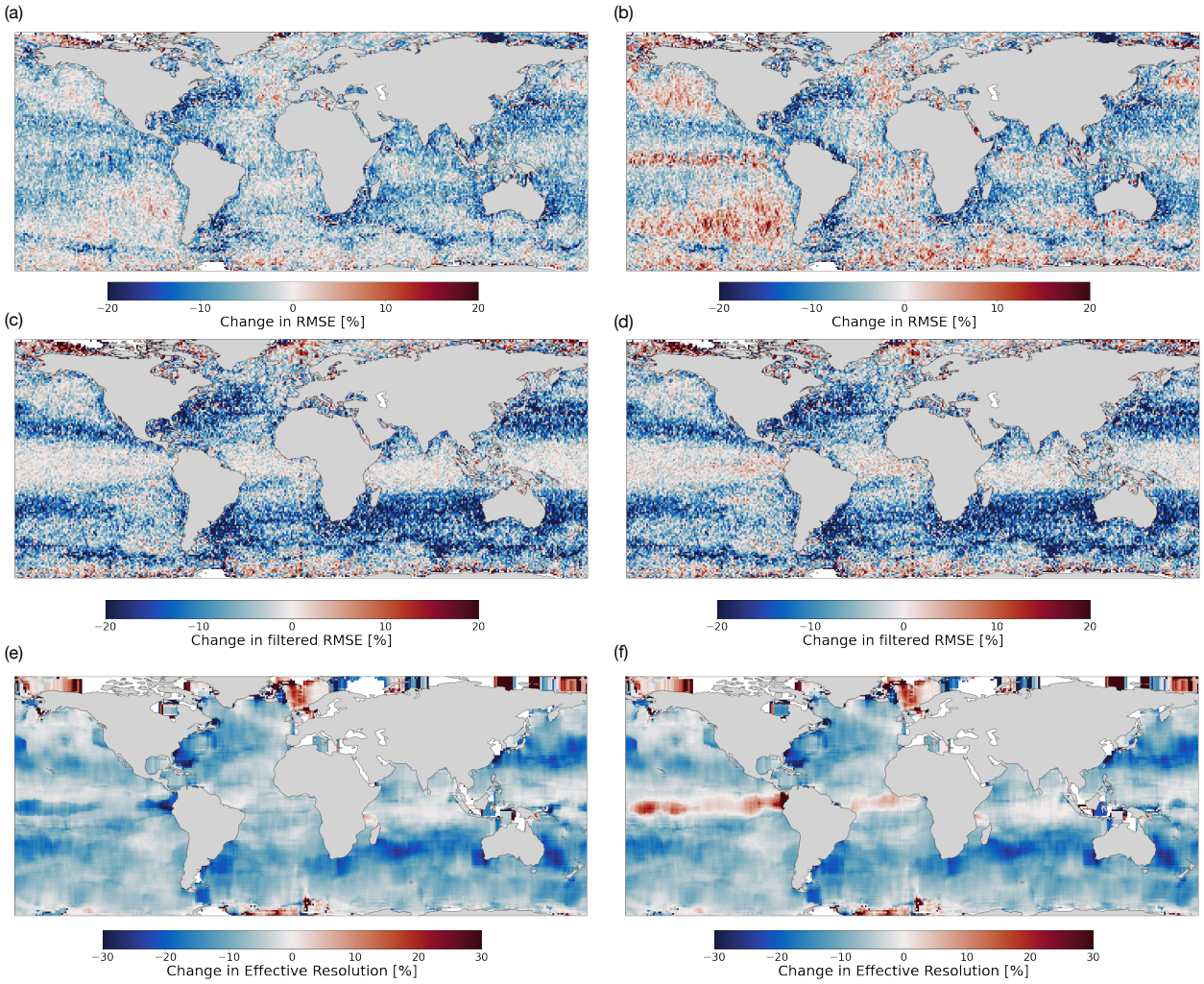

Extended Data Figure 1. (a) Change in RMSE for SimVP SSH-SST compared to MIOST (geos.) (b) Same as (a) but for SimVP SSH-SST compared to MIOST (geos. + waves). (c) Change in RMSE for wavelengths between 70 and 250km for SimVP SSH-SST compared to MIOST (geos.). (d) Same as (c) but for SimVP SSH-SST compared to MIOST (geos. + waves). (e) Change in smallest resolved wavelength for SimVP SSH-SST compared to MIOST (geos.). (f) Same as (e) but for SimVP SSH-SST compared to MIOST (geos. + waves).

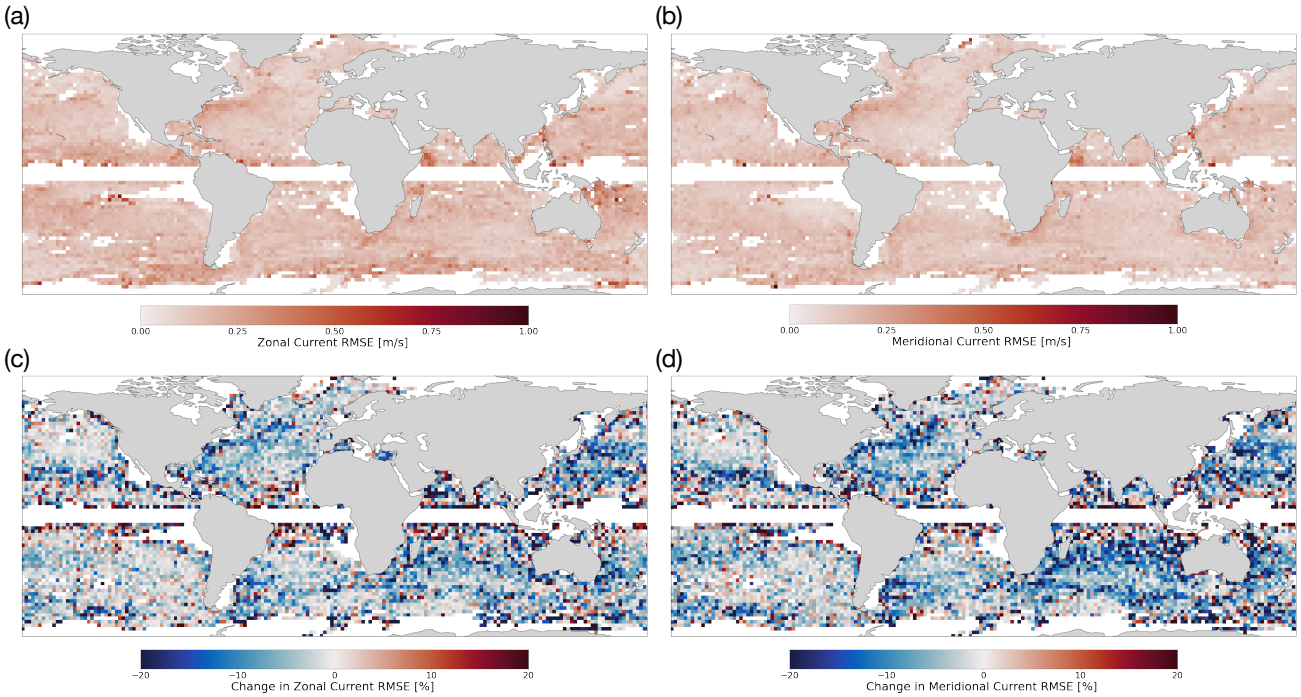

Extended Data Figure 2. (a) RMSE of SimVP SSH-SST zonal surface geostrophic currents compared to surface drifters. (b) Same as (a) but for the meridional currents. c, Change in zonal current RMSE for SimVP SSH-SST compared to DUACS. (d) Same as (c) but for the meridional currents.

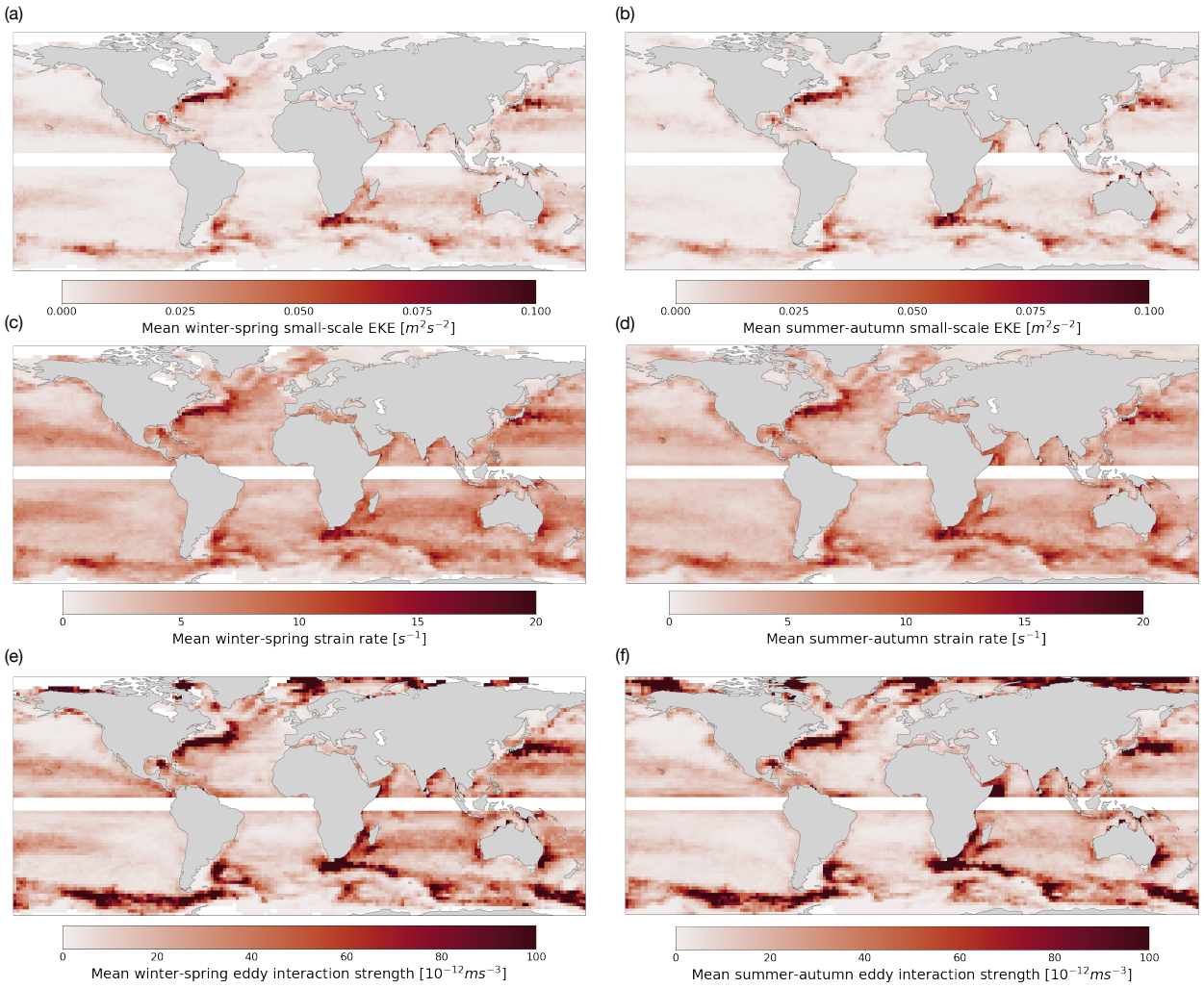

Extended Data Figure 3. Absolute values of the fields in Figure 4 calculated from SimVP SSH-SST maps.

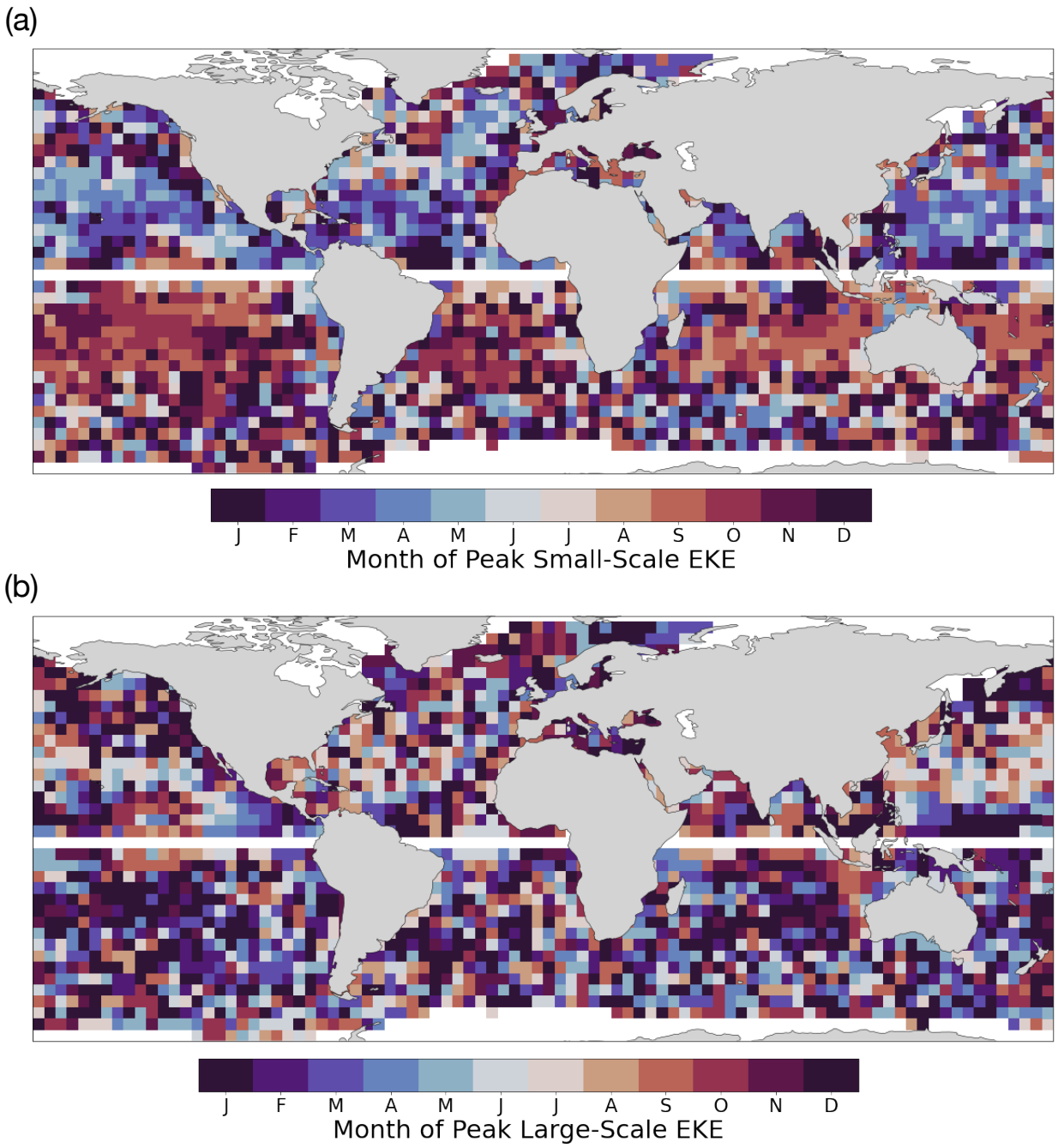

Extended Data Figure 4. (a) Month of the year in which small-scale (wavelengths below 250km) EKE peaks. (b) Same as (a) but for the large-scale EKE.

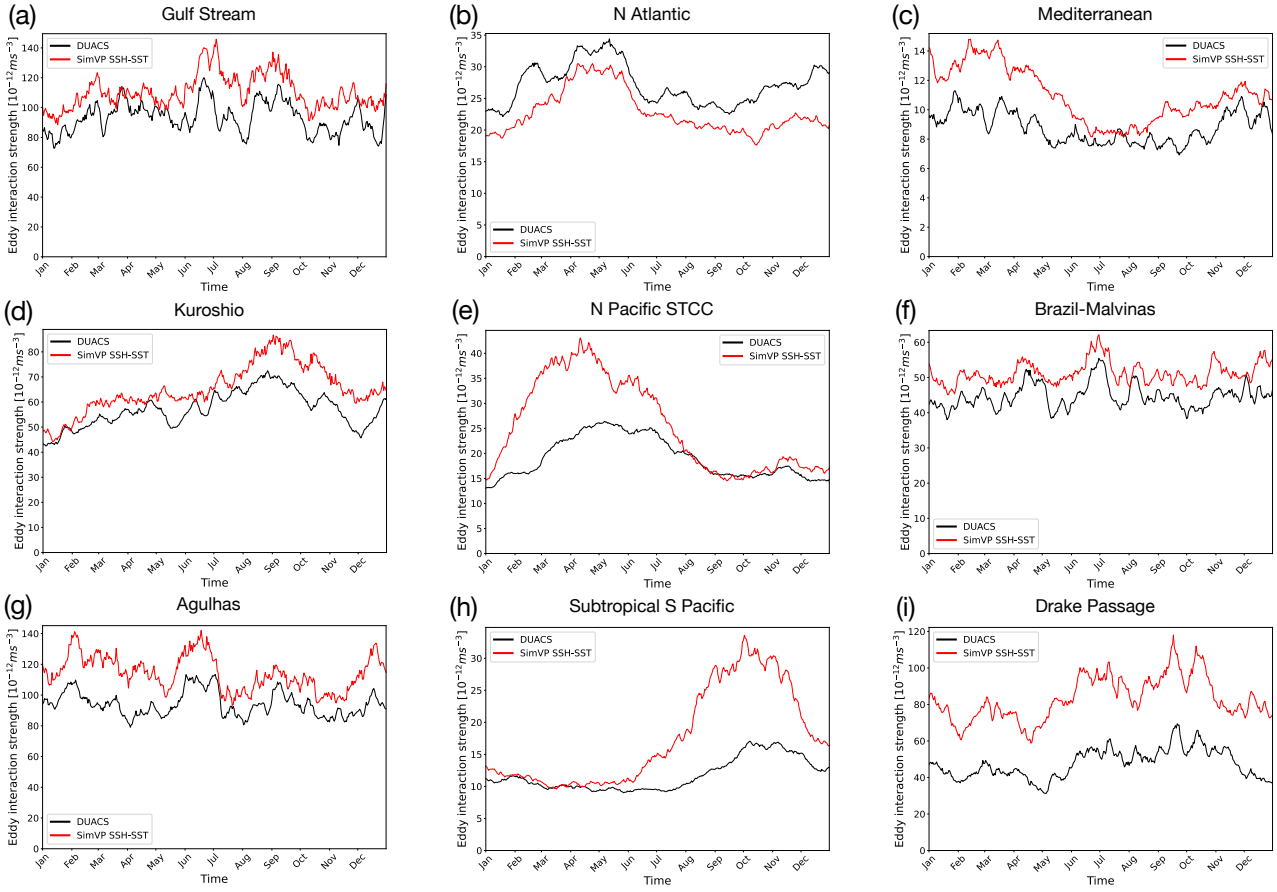

Extended Data Figure 5. Time-series' of the non-linear eddy interaction strength for SimVP SSH-SST and DUACS averaged over the regions defined in Extended Data Table 1 (Equatorial Pacific excluded since geostrophy breaks down here).

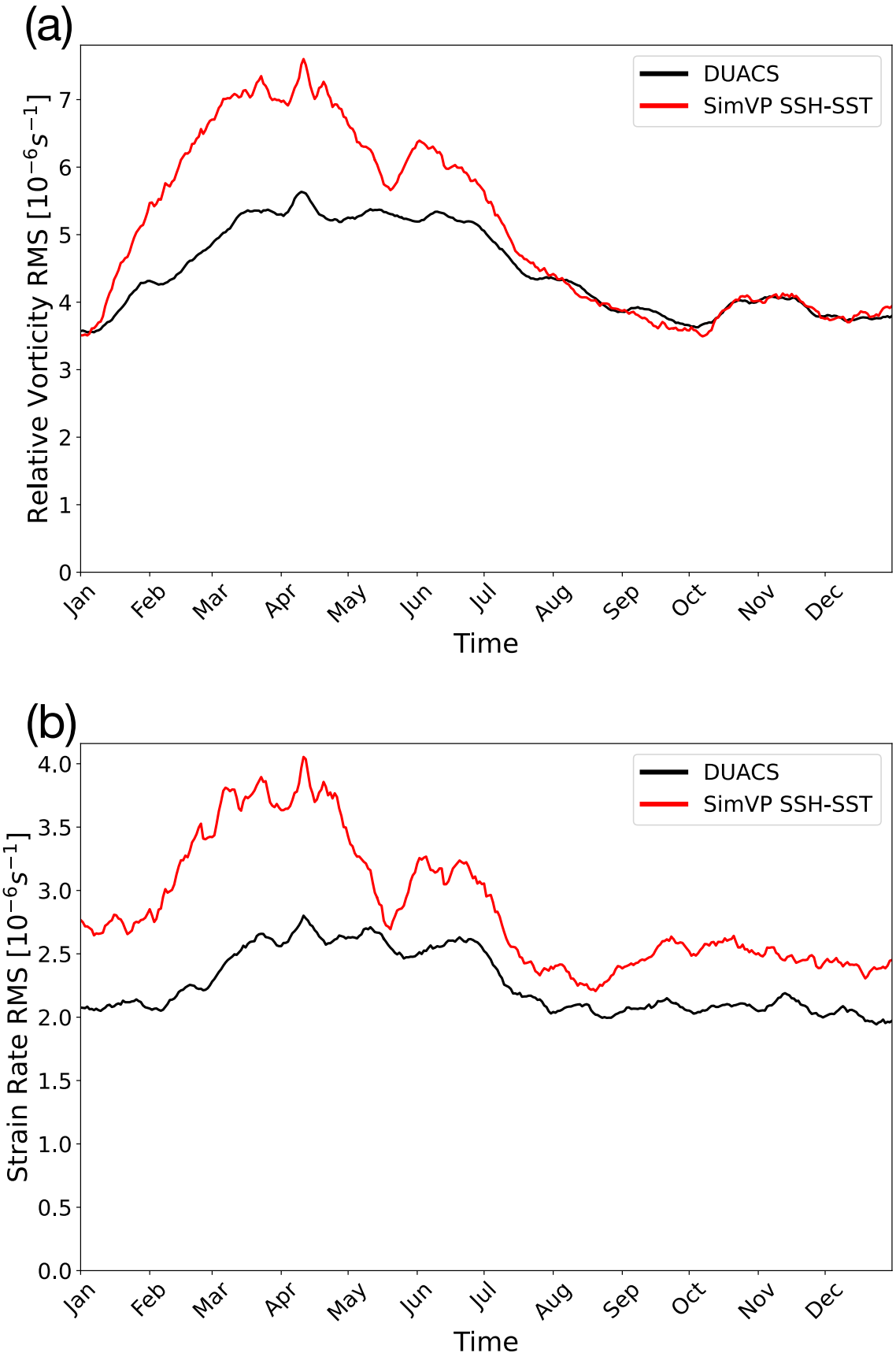

Extended Data Figure 6. Time-series' of the root-mean-square (RMS) value of (a) relative vorticity and (b) strain rate in the Subtropical North Pacific from SimVP SSH-SST and DUACS.

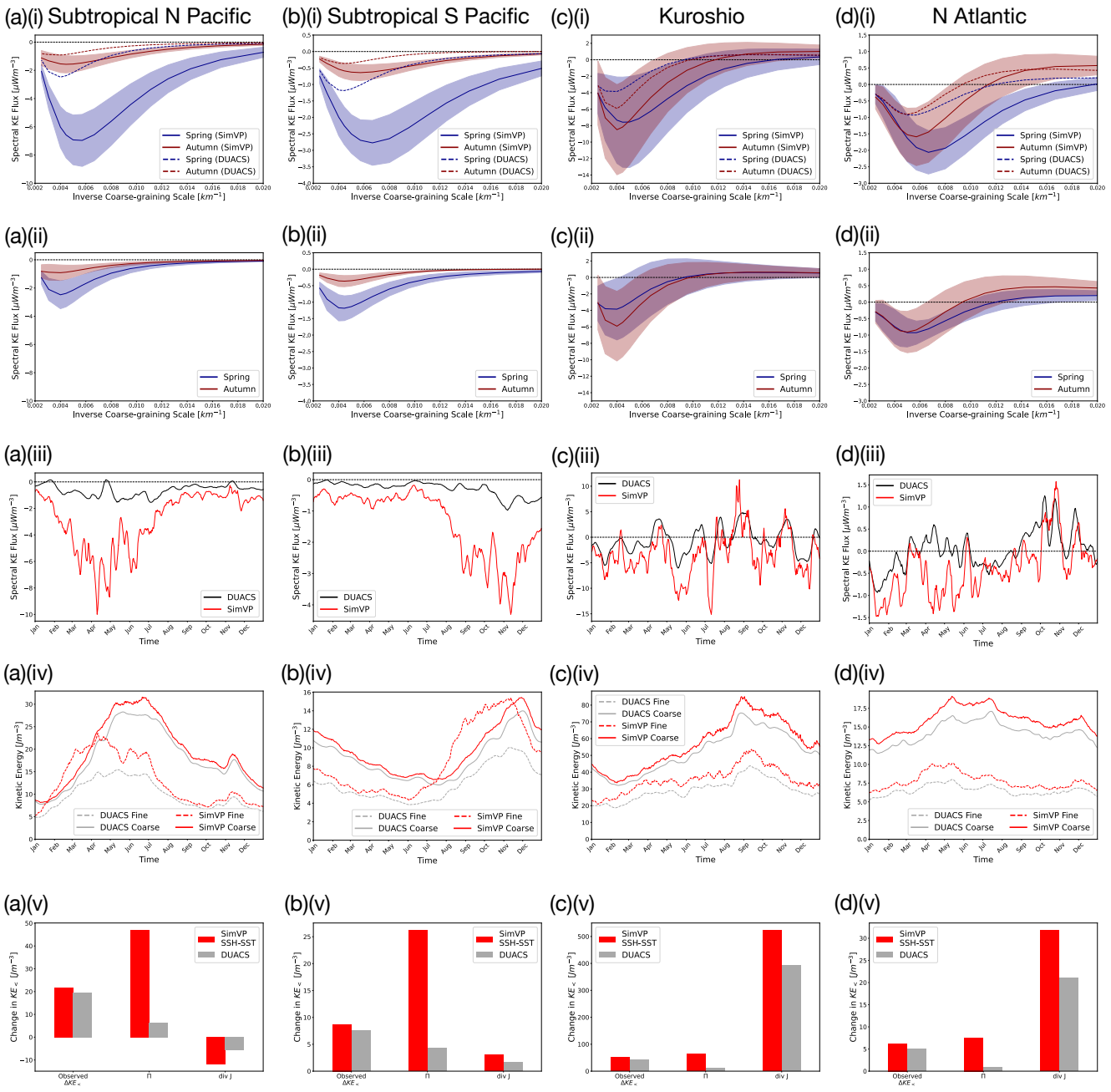

Extended Data Figure 7. (a) Subtropical North Pacific (149-161E, 19-31N). (i) Mean (solid lines) and standard deviation (shading) of KE cascade from SimVP SSH-SST surface currents for the seasons of maximum (Spring) and minimum (Autumn) upscale cascade with mean DUACS cascades for reference (dashed lines). (ii) Same as (i) but from DUACS. (iii) Time-series of KE cascade across 250km for both SimVP SSH-SST and DUACS. (iv) Time-series of coarse- and fine-scale KE (above and below coarse-graining scale of 125km respectively) from both SimVP SSH-SST and DUACS. (v) Change in $KE_<$ (coarse-scale KE) from its wintertime minimum to its summertime maximum compared to the diagnosed contribution from the KE cascade ($-\int \Pi dt$), and the spatial transport of coarse-scale KE ($-\int \nabla \cdot J dt$) for both SimVP SSH-SST and DUACS. (b)(i-v) Same as (a)(i-v) but for the Subtropical South Pacific (194-206E, 19-31S). (c)(i-v) Same as (a)(i-v) but for the Kuroshio (153-167E, 29-41N). (d)(i-v) Same as (a)(i-v) but for the North Atlantic (322-338E, 39-51N) and with the dividing coarse-graining scale between fine- and coarse-scale KE reduced to 80km.

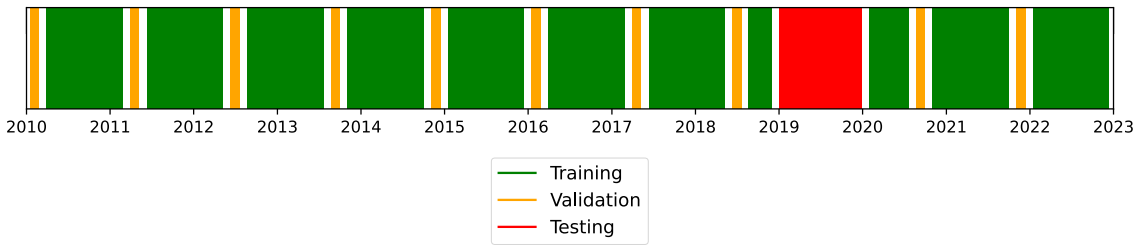

Extended Data Figure 8. Partitioning of dates between training, cross-validation, and testing when training neural network for SSH mapping.